Origin of subsurface voids in additively manufactured Ni-base alloy IN625 induced by oxidation

Corrosion Science 271 (2026) 114147

Contents lists available at ScienceDirect

Corrosion Science

journal homepage: www.elsevier.com/locate/corsci

Origin of subsurface voids in additively manufactured Ni-base alloy IN625 induced by oxidation

Anton Chyrkin [a,*], Dmitry Naumenko [b]

[a] Chalmers University of Technology, Department of Chemistry and Chemical Engineering, Kemivägen 10, Gothenburg 412 54, Sweden
[b] Forschungszentrum Jülich GmbH, Institute for Energy Materials and Devices (IMD-1), Leo-Brandt-Straße, Jülich 524 25, Germany

ARTICLE INFO

Keywords:
Ni-base alloy
Additive manufacturing
IN625
Oxidation
Porosity
Vacancy injection

ABSTRACT

Additively manufactured (AM) high-temperature alloys often develop subsurface porosity during oxidation at high temperatures. These voids in the surface-near region can oxidize and cause intergranular oxidation attack. The origin of the oxidation-induced porosity has been studied in AM as well as in the conventionally manufactured (CM) alloy IN625. The alloy specimens were exposed in air, Ar-4%H_2-2%H_2O, and Cr/Cr_2O_3 Rhines pack (RP) for up to 1000 h at 900 and 1000 °C. The alloys were also welded with pure nickel to simulate interdiffusion, i.e., Cr loss without oxidation. The diffusion couples were annealed in vacuum for up to 1000 h at 900 and 1000 °C. The CM specimens did not form significant micron-scale subsurface voids while the AM specimens developed extensive subsurface porosity (4–7 vol%) in the oxidation experiments and very limited porosity (less than 1 vol%) in the interdiffusion couples. No voids developed in the RP exposures. Vacancy injection was demonstrated to be the primary trigger of the subsurface porosity in AM.

1. Introduction

Industrial applications such as power generation, heat processing, petrochemical refineries, aeronautics, etc. require structural materials which combine high creep resistance with high environmental resistance against oxidation and/or corrosion at high temperatures [1]. FeNiCr- and NiCr-base high-temperature alloys such as austenitic stainless steels and Ni-base superalloys are currently the state-of-the-art materials for the above-mentioned applications to manufacture structural components as well as protective claddings and coatings.

Additive manufacturing (AM) of metallic materials has recently created a separate family of the high-temperature alloys as AM offers significantly more flexible shaping options as well as much more efficient waste management compared to the traditional manufacturing routes [2–5]. The AM process, most commonly powder bed fusion - laser beam (PBF-LB), involves fast solidification due to high cooling rates and results in anisotropic and highly inhomogeneous, dendritic microstructures [6] which may significantly compromise creep and fatigue strength of the alloys. Recent studies of e.g. AM Ni-base alloy 625 [7,8] and alloy 718 [9–11] demonstrate, however, that optimization of HIP and post-manufacturing heat-treatment leads to creep rates comparable with those measured for the respective conventionally manufactured (CM), wrought or forged alloys.

On the other hand, the oxidation resistance of AM alloys is systematically reported to be inferior to the performance of the CM counterparts [12–32]. The main phenomenon behind the enhanced corrosion of AM Ni-base alloys is intergranular oxidation attack (IGOA), i.e., formation of internal Cr_2O_3 in alloys which contain 20–25 wt% Cr and are expected to grow external Cr_2O_3 scales. IGOA is not limited only to AM high-temperature alloys. The occurrence of IGOA has been previously reported for commercial [33,34] and model NiCr-base alloys [35–38] during oxidation above 1000 °C.

A common feature for IGOA occurring in both CM and AM alloys is the abundant subsurface porosity [39]. This porosity is caused by the local supersaturation of vacancies arising due to either vacancy injection related to incorporation of metal atoms into the oxide scale or Kirkendall effect related to non-balanced fluxes of alloy elements within the metal upon Cr-depletion. As the nature of oxidation-induced porosity in AM alloys is not fully understood, the following questions are addressed in the present study:

i) Which of the above void formation mechanisms is most relevant for AM alloys?
ii) Is the void formation mechanism for AM different than for CM?

* Corresponding author.
E-mail address: chyrkin@chalmers.se (A. Chyrkin).

https://doi.org/10.1016/j.corsci.2026.114147
Received 13 April 2026; Received in revised form 1 July 2026; Accepted 29 July 2026
Available online 5 August 2026

iii) Why do these subsurface voids oxidize [35,37,38,40]?
iv) Is the void oxidation mechanism the same for CM and AM alloys?

The goal of the present study is to establish the exact mechanism of void formation in additively manufactured Ni-base alloy IN625 during oxidation clearly differentiating between the generic effects such as vacancy injection as well as Kirkendall effect and the effects introduced by additive manufacturing. To this end, two types of experiments simulating the oxidation-induced Cr-loss from the AM and CM alloy were undertaken. First, AM and CM alloy IN625 specimens were oxidized in air and Cr/Cr_2O_3 Rhines pack. In the latter environment, the oxygen potential set by the Cr/Cr_2O_3 equilibrium prevents the external Cr_2O_3 from forming while the other alloy elements with a higher affinity for oxygen such as Al, Mn, Si, Ti can oxidize. This experiment allows exploring the role of internal oxidation in IGOA. In the second type of experiments, Ni-IN 625 diffusion couples were manufactured for CM and AM and annealed in vacuum repeating the testing conditions (temperature and time) for the oxidation experiments. The diffusion couple experiments allow simulation of the Cr-loss from the CM and AM alloys independent of oxidation. In the interdiffusion experiment, however, vacancy injection is avoided as the Cr-loss compensated by counter-diffusion of Ni.

2. Experimental procedure

2.1. Materials

Conventionally manufactured (CM) alloy IN625 was a forged bar supplied by Huntington Alloy Corp. The same CM alloy batch was studied in [41]. Additively manufactured (AM) alloy IN625 was fabricated by the powder bed fusion - laser beam (PBF-LB) technique. The manufacturing details are described in detail in [42]. AM was manufactured from the same CM batch to minimize the differences in chemical composition between CM and AM. The chemical compositions of AM and CM alloy IN625 obtained by ICP-OES are given in (Table 1). As no significant anisotropy of oxidation behavior has been detected for this AM material [42], only transversally sectioned (AM-Z) AM alloy specimens were used in the present study.

The microstructures of as-printed AM alloy IN625 and conventionally manufactured (CM) forged alloy IN 625 are demonstrated in Fig. 1 and Fig. 2.

The inverse pole figure (IPF) EBSD maps show the grain structure in the longitudinal (Fig. 1a) section of the AM alloy. The characteristic AM microstructure consisting of 30–40 μm wide vertical melt pools aligned along the build axis Z has been previously reported for this alloy in e.g. [21,42,43]. The forged CM alloy IN 625 (Fig. 1b) contains equiaxed grains with the average grain size of 12 μm [41].

High-magnification BSE SEM images in Fig. 2a demonstrate that the AM material consists of dendritic and cellular structures, i.e., subgrains 100–200 nm in diameter, resulting from a rapid solidification. These submicron microstructures are typical for AM alloys including alloy IN625 [44].

2.2. Oxidation tests

All alloy coupons of AM and CM IN625 were machined to 10x10x2 mm^3 dimensions. The surfaces were ground with SiC papers to 1200 grit.

The CM and AM specimens were exposed in air for up to 1000 h at 900 °C. Discontinuous exposures were performed in a horizontal tube furnace (⌀ 44 mm) at 900 °C for up to 1000 h. The temperature calibration was performed by an external Pt/Rh-thermocouple to establish a 4 cm wide zone of stable temperature in the furnace. Selected CM and AM alloy coupons were ground to 0.3 mm thickness to study the effect of thickness on oxidation behavior. The final surface finish of the thin foil specimens was also 1200 grit.

The exposures were carried out in quartz tubes in a horizontal tubular furnace in stagnant lab air. The specimens were degreased in ethanol and acetone prior to exposure and directly introduced into the hot zone of the tube furnace. After exposures, the specimens were removed from the hot zone of the furnace and cooled down in air.

The exposures in $Ar-4\%H_2-2\%H_2O$ gas mixtures were carried out in an alumina tube in a horizontal tubular furnace. The $Ar-4\%H_2$ gas mixture supplied by Linde Gas was bubbled through a humidifier kept at 17.5 °C. The oxygen partial pressure, pO_2, in this gas mixture is 1.5×10^{-17} bar at 900 °C and 7.9×10^{-16} bar at 1000 °C. The alloy specimens were introduced into a cold furnace, flushed with the dry $Ar-4\%H_2$ gas for 1 h and heated at 10 K min^{-1} to reach the exposure temperature. The humidification was turned on once the furnace reached the target temperature. The cooling rate was 10 K min^{-1} as well. The gas flow rate was set at 200 ml min^{-1}.

The mass gain curves were obtained by gravimetric measurements prior and after the exposures using Mettler Toledo XP6 microbalance with a 1 μg resolution.

2.3. Rhines pack exposures

The Rhines pack (RP) technique [45] is a special type of experiment in which an alloy specimen is sealed together with a M/MO_n (M is typically Fe and/or Ni) powder mixture called pack in an evacuated quartz capsule (see Figure S1 in **Data Supplement**). The pack buffers oxygen in the evacuated environment and sets its partial pressure pO_2 at the level of dissociation of MO_n. The RP technique allows exposures in which only the alloying elements with higher affinity for oxygen than M are oxidized while the base metal remains inert. Another advantage of RP is the absence of additional species such as carbon or hydrogen as it is the case in the H_2/H_2O and CO/CO_2 gas mixtures [46], respectively, which are commonly used to create atmospheres with low pO_2 [47,48]. RP is mainly used for studies of internal oxidation [47,48] and measurements of oxygen permeability [47,49] but also in studies of external Cr_2O_3 scaling [50,51]. Most reported RP studies were carried out in Fe/FeO_x and Ni/NiO RPs. To the best knowledge of the authors, only one study describing oxidation in Cr/Cr_2O_3 RP is available in literature [52].

In the present work, the Cr/Cr_2O_3 pack made of metal/oxide powder was substituted by Cr_2O_3 thermally grown on a binary alloy Ni−30Cr supplied by MWH Hauner GmbH (Röttenbach, Germany). The as-received 0.6 mm thick sheet was cut in triangular granules (no longer than 2 mm in one dimension). The alloy granules were oxidized in $Ar-4\%H_2-2\%H_2O$ for 200 h at 1000 °C. The average oxygen uptake for 3 g of granules was 30 mg. The oxidized granules were mixed with unoxidized alloy material in ratio 3: 2. The pO_2 established by the Cr/Cr_2O_3 mixture is 5.3×10^{-25} bar at 900 °C.

The alloy coupons of CM and AM alloy IN625 were put together with 5 g of the Cr/Cr_2O_3 pack in a 16 mm outer diameter (OD) quartz tube and sealed under vacuum (10^{-5} mbar). The sealed quartz capsules were exposed in a horizontal tube furnace with a 4 cm wide stable hot zone at 900 °C for 100, 300 and 1000 h. The capsules were immediately introduced into the hot zone of the furnace. The capsules were rapidly removed from the hot zone after exposure and cooled in air.

Table 1
Chemical composition of as-forged CM and AM alloy IN625 in wt% determined by ICP-OES and IR combustion analysis.

Alloy	Ni	Cr	Mo	Nb	Fe	Cu	Mn	Ti	Al	Si	C	O	N
CM	Bal.	21.5	9,1	3.5	3.61	0.19	0.11	0.33	0.32	0.27	0.02	0.001	0.013
AM	Bal.	21.6	9.1	3.23	3.60	0.31	0.10	0.33	0.30	0.23	0.06	0.019	0.044

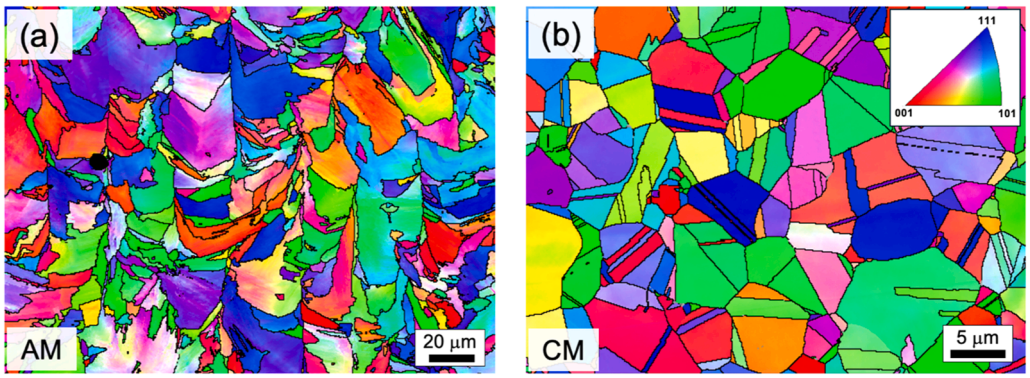

Fig. 1. EBSD IPF-Z maps for as-printed AM (a) and CM (b) alloy IN625. Note the magnification difference in scale bars.

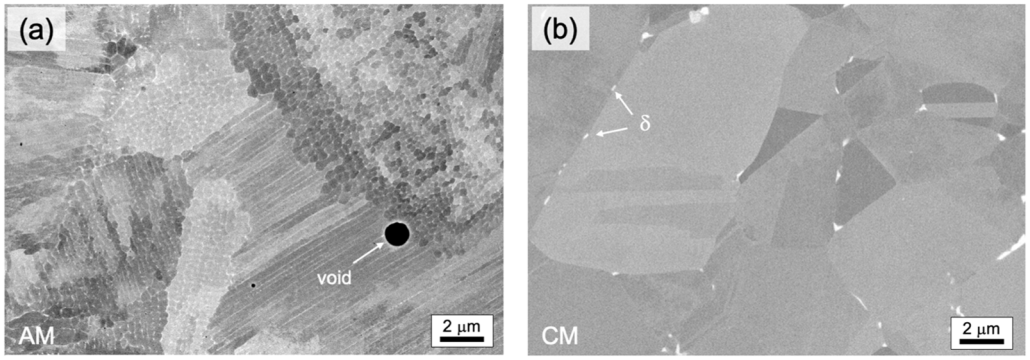

Fig. 2. BSE SEM images of as-printed AM (a) and CM (b) alloy IN625.

2.4. Diffusion couples

The CM-Ni-AM diffusion couple was manufactured using a clamp technique described in [53]. All materials were machined as 21 mm OD discs with 2 mm thickness. The CM disc was machined from the forged bar of alloy IN625. The disc of 99.995% pure nickel was supplied by MWH Hauner GmbH (Röttenbach, Germany). The Ni disc was annealed for 100 h at 1050 °C in flowing Ar−4%H_2 to coarsen the grains and remove the remnant impurities. The AM disc was built as a 3 mm thick cylinder (21 mm OD) and was ground to 2 mm thickness with SiC papers. The AM disc was used for welding in as-built condition. All three discs were ground to P4000 grit with SiC papers and polished to 1 μm surface finish. The AM and CM discs were polished on one side while both surfaces of the Ni were polished for welding. The diffusion couple was assembled as demonstrated in Figure S2 in **Data Supplement** in the following order: CM – Ni – AM. The diffusion couple was placed between two circular clamp flanges (40 mm OD) made of austenitic 310 L steel. The clamp was tightened with six 55 mm long screws and nuts through equally spaced orifices in the flanges (see Figure S2a). The clamp was placed in a 43 mm ID quartz tube inside a tubular furnace and was heated to 900 °C under flowing Ar−4%H_2 for 2 h. The gas flow rate was set at 200 ml min^{-1}. The clamp was readily removed from the furnace and cooled down in air. After welding, the diffusion couple was a 6 mm thick cylinder which was sectioned in 8 symmetrical pieces. One diffusion couple was metallographically cross-sectioned to verify a proper welding of all interfaces. Diffusion couples were sealed in quartz capsules under vacuum (10^{-5} mbar) and subsequently exposed to reach 24 h, 100 h, 300 h and 1000 h of total exposure time at 900 °C and 1000 °C. After exposures, the diffusion couples were cross-sectioned and metallographically examined for interdiffusion.

2.5. Ni-coating

A set of CM and AM specimens were electrochemically plated with Ni. The alloy specimens were polished to 1 μm surface finish and degreased in acetone prior to plating. The Ni-plating bath was an aqueous solution of 240 g $NiSO_4$, 17 g KCl and 42 g $(NH_4)_2SO_4$ per 2 L of deionized water. The anode was a plate of pure Ni. The bath was magnetically stirred and held at 50 °C. The voltage was 1.8 V achieving the current density of approximately 50 mA/cm^2. The plating time was 15 min. The resulting thickness of the Ni layer was 5 μm. The Ni-plated specimens were sealed under high vacuum in a quartz capsule and annealed for 24 h at 900 °C. The annealed Ni-coated specimens were sectioned for microstructural analyses.

2.6. Microstructural characterization

Electron backscatter diffraction (EBSD) maps were obtained on as-received materials using a Zeiss Ultra 55 field emission gun (FEG) scanning electron microscope (SEM) equipped with an HKL Channel 5 EBSD detector. An FEI Quanta 200 SEM equipped with an Oxford X-max 80 energy dispersive X-ray spectrometer (EDX) was employed for pre- and post-exposure analysis. Aztec software was used to evaluate the EDX data. The exposed specimens were hot mounted into PolyFast mounting resin (Struers, Denmark). Prior to hot mounting, the specimens were gold sputtered and electroplated with nickel as described above. Cross-sections were prepared by a conventional metallographic preparation route. The mounted specimens were mechanically ground with SiC papers to 4000 grit and subsequently polished with diamond pastes (0.25 μm) and colloidal silica (≈50 nm).

3. Results

3.1. Oxidation kinetics: effect of thickness

Fig. 3a shows weight change curves for CM and AM alloy IN625 discontinuously exposed in air at 900 °C and in Ar−4%H_2−2%H_2O at 1000 °C. The CM and AM alloy specimens were 2 mm and 0.3 mm thick. The weight change curves in Fig. 3a reveal two important observations: i) there is no measurable difference in oxidation rate between CM and AM in agreement with our previous work [42] and ii) there is virtually no thickness dependence of the oxidation rate reported for ferritic stainless steels [54,55] and even for NiCr-base alloys at 1000 °C [56]. No acceleration of oxidation of thin foils was found at 900 °C while a marginally higher oxidation rate was recorded for the thin foil (0.3 mm) of CM IN625 compared to the 2 mm thick CM specimen. No effect of thickness was detected for the AM specimens.

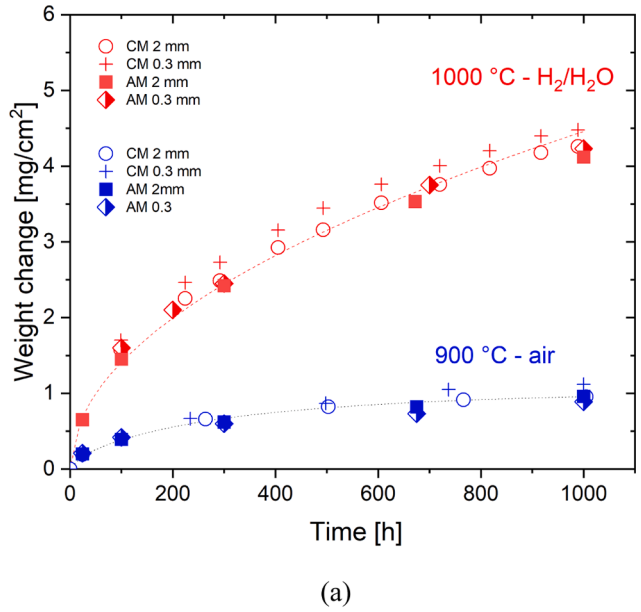

Fig. 3. Weight change curves for AM and CM alloy IN625 exposed in (a) air, Ar−4%H_2−2%H_2O and (b) Cr/Cr_2O_3 Rhines pack for up to 1000 h at 900 and 1000 °C. Figure (a) compares thick (2 mm) specimens with thin (0.3 mm) foils of both CM and AM. Figure (b) compares oxidation in Cr/Cr_2O_3 Rhines pack (squares) with air oxidation (circles) at 900 °C. Lines denote parabolic fitting curves.

3.2. Oxidation kinetics: exposures in Cr/Cr_2O_3 Rhines pack

Fig. 3b demonstrates oxygen uptake for CM and AM alloy IN625 discontinuously measured during exposures in air and Cr/Cr_2O_3 Rhines pack (RP) for up to 1000 h at 900 °C. It is remarkable that the air exposed specimens demonstrated significantly higher oxygen uptakes compared to the RP specimens. This result is expected because an external Cr_2O_3 scale cannot grow in the Cr/Cr_2O_3 environment [52]. The oxygen uptake in RP is contributed by the alloy elements with a high oxygen affinity such as Ti, Al, Si, Mn, etc. able to oxidize at the decomposition pressure, pO_2, of Cr_2O_3. Another important observation is the negligible difference in oxidation kinetics of the CM and AM in both environments.

Fig. 4 shows back scattered electron (BSE) SEM images of cross-sectioned CM and AM alloy IN625 specimens exposed in air for 100, 300 and 1000 h at 900 °C. The CM alloy specimens developed a well-documented morphological oxidation pattern known for IN625 [41]: (i) external Cr_2O_3 scales, (ii) internal precipitation of Al_2O_3 at the alloy GBs, (iii) the intermetallic phase δ-Ni_3(Nb,Mo) at the oxide-metal interface, (iv) a precipitate free zone with coarsened grains.

The AM specimens grew an external Cr_2O_3 scale followed by a characteristic re-precipitation of the δ-phase. The main difference between CM and AM is the subsurface porosity in the oxidation affected zone of the AM specimens. The Cr_2O_3 scales on both CM and AM are equally thick and corrugated.

Fig. 5 presents BSE SEM images of cross-sectioned CM and AM alloy IN625 specimens exposed to Ar−4%H_2−2%H_2O for 100, 300, and 1000 h at 1000 °C. At this temperature, the δ-phase is not stable in the alloy; however, it precipitates at the oxide-metal interface as previously reported in [41]. The Cr_2O_3 scales formed on CM are thicker and smoother compared with the air-grown oxide scales shown in Fig. 4. In contrast, the Cr_2O_3 scales formed on AM (bottom row in Fig. 5) appear more undulated than those formed on CM. Unlike the observations at 900 °C (Fig. 4), sporadic spherical voids are observed in the oxidation affected zones following exposure at 1000 °C. The voids in the AM

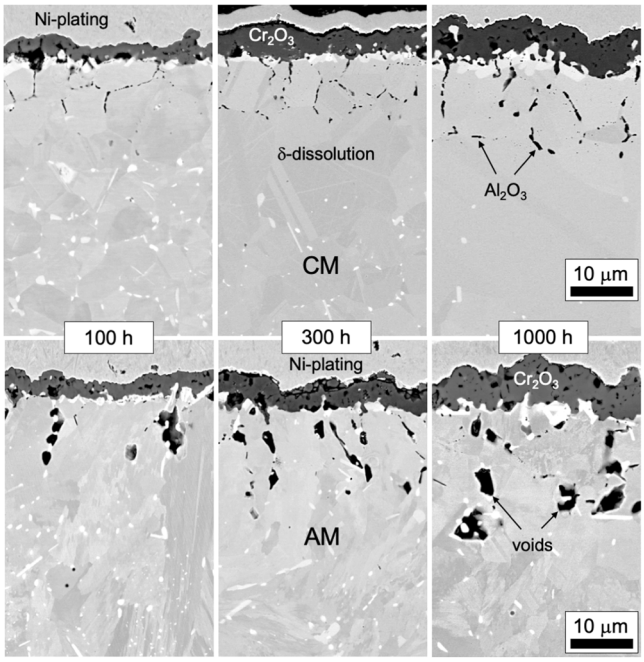

Fig. 4. BSE SEM images of cross-sectioned CM (upper row) and AM (bottom row) alloy IN625 specimens after 100, 300 and 1000 h of oxidation in air at 900°C.

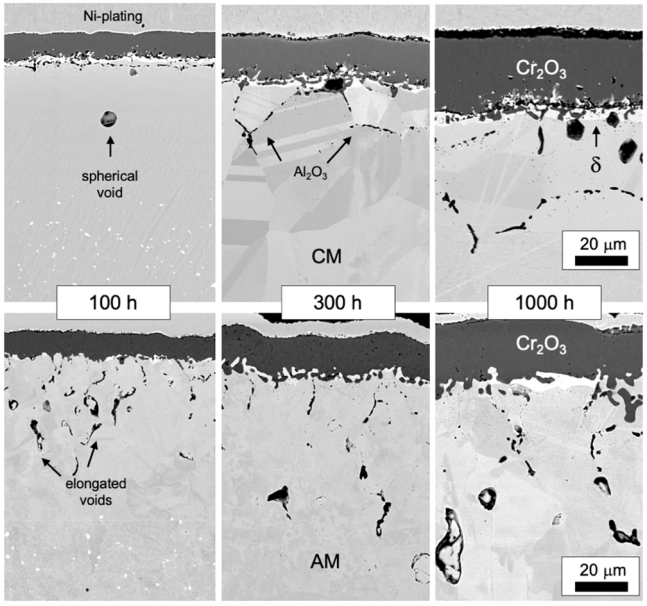

Fig. 5. BSE SEM images of cross-sectioned CM (upper row) and AM (bottom row) alloy IN625 specimens after 100, 300 and 1000 h of oxidation in Ar−4% H_2−2%H_2O gas mixture at 1000 °C.

specimens are elongated and significantly more abundant than in CM.

Fig. 6 demonstrates a collage of BSE SEM images of cross-sectioned CM and AM alloy IN625 specimens exposed in Cr/Cr_2O_3 Rhines Pack (RP) for 100, 300 and 1000 h at 900 °C. In contrast to experiments in air, the RP exposures resulted almost exclusively in internal oxidation. Discontinuous islands of external oxide contained Ti, Mn and Si according to the EDX analysis (not shown here) and traces of Cr. Some limited oxidation of Cr was most probably due to residual water contained by quartz of the sealing capsules. The thickness of the external oxide was less than 1 μm in all RP exposures. Similar to the air exposures, the CM specimens exposed in RP revealed an internal oxidation zone (IOZ) of Al, i.e., Al_2O_3 precipitations at the alloy GBs. More remarkably, the IOZ was clearly visible in the AM specimens exposed in RP compared to the air exposed AM samples Fig. 4. The observation of IOZ in the air exposed AM specimens was obstructed by the abundant subsurface porosity (bottom row in Fig. 4). The most important result of the RP exposures is the absence of the subsurface porosity in the AM specimens exposed in RP (Fig. 6) compared to the air exposed AM specimens (Fig. 4).

The kinetics of the IOZ propagation at 900 °C in the air exposed CM as well as the AM and CM specimens exposed in RP are summarized in Fig. 7. Additionally, the data from the present study were compared with the IOZs obtained in the same alloy batch during exposures in Ar−4% H_2−2%H_2O at 900 °C [41]. The internal oxidation kinetics are in very good agreement with the previous measurements [41]. Most importantly, the IOZ growth kinetics are very similar for all experimental conditions irrespective of the exposure environment (air, H_2/H_2O or RP) as well as the metallurgical state of the alloy (CM or AM).

3.3. *Subsurface porosity: effect of thickness*

BSE SEM images of the sectioned AM IN625 specimens after 1000 h oxidation at 900 and 1000 °C presented in Fig. 8 demonstrate the effect of specimen thickness on the subsurface porosity. The oxide scale thickness at 900 °C (Fig. 8a,b) and 1000 °C (Fig. 8c,d) is independent of the specimens thickness, in agreement with the thermogravimetric results in Fig. 3a. Similar to the Cr_2O_3 thickness, the widths of the porosity zone is not affected by the specimens thickness. However, the total volume of the voids appears to be larger in the thin specimens (Fig. 8a,c) compared to the thick ones (Fig. 8b,d).

Fig. 9 summarizes the porosity measured in the oxidation-affected zones of thin (0.3 mm) and thick (2 mm) AM IN625 specimens oxidized for up to 1000 h at 900 and 1000 °C, as well as in the interdiffusion zones of Ni–IN625 diffusion couples (DC) annealed under the same conditions. The void surface area was determined from low-magnification SEM images. The void volume fraction was assumed to be equal to the measured area fraction.

Porosity is systematically higher at 900 °C (up to 6.5% in thin foils) than at 1000 °C (up to 4.5% in 2 mm thick coupons). Remarkably, porosity is greater in the thinner specimens (0.3 mm) than in the thicker specimens (2 mm). Only minor porosity (0.5–0.8%) is observed in the interdiffusion zones of the diffusion couples.

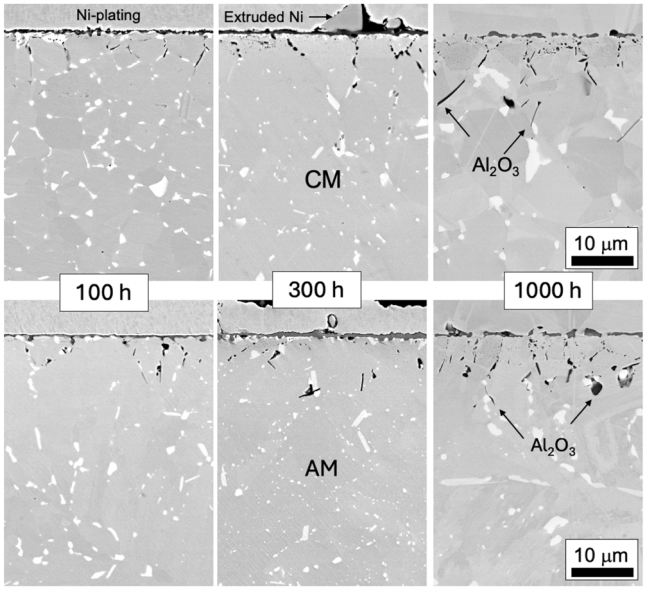

Fig. 6. BSE SEM images of cross-sectioned CM (upper row) and AM (bottom row)) alloy IN625 specimens after 100, 300 and 1000 h of exposure in Cr/Cr_2O_3 Rhines pack at 900°C.

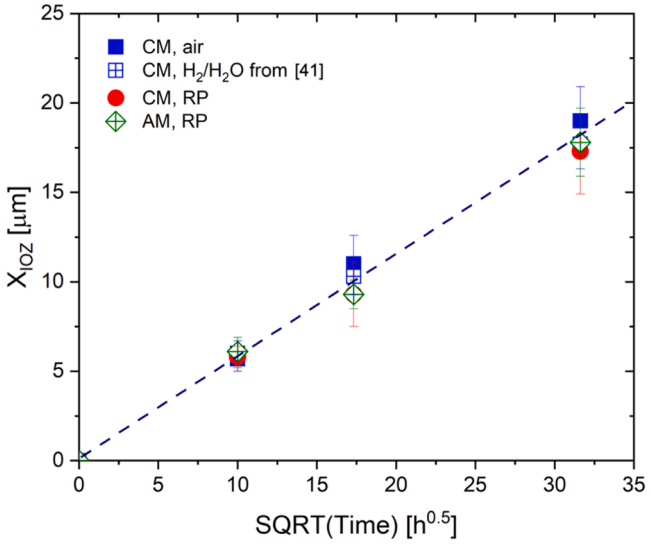

Fig. 7. Kinetics of internal oxidation of Al in CM (full symbols) and AM (empty symbols) alloy IN625 during exposures in air, Ar−4%H_2−2%H_2O gas mixture (literature data from [41]) and Cr/Cr_2O_3 Rhines pack at 900 °C.

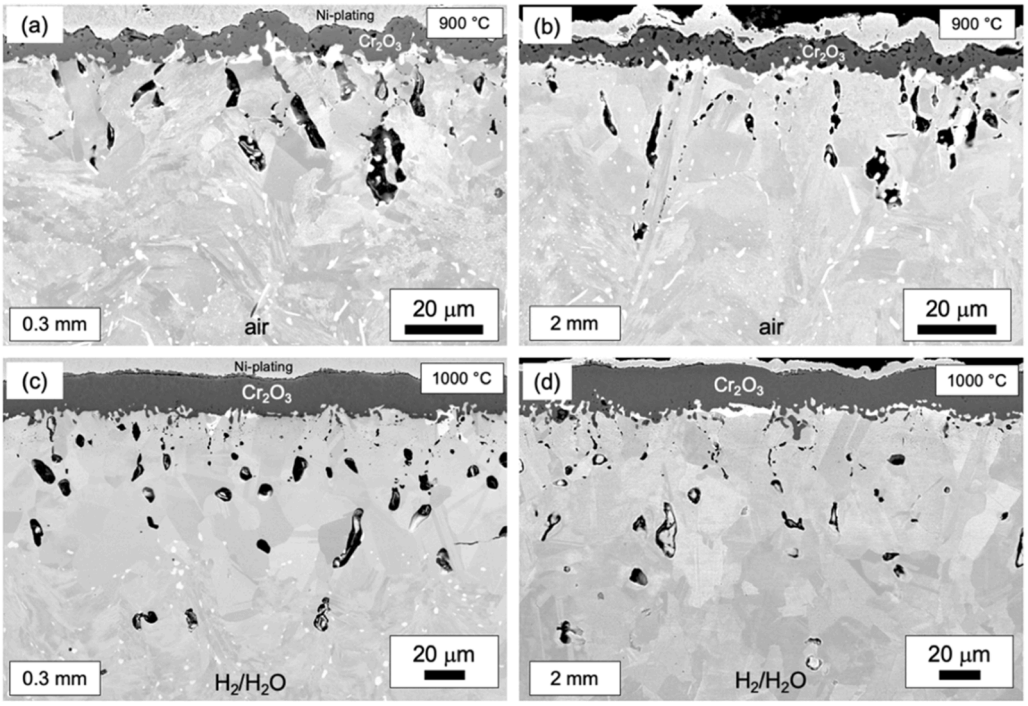

Fig. 8. BSE SEM images comparing subsurface porosity in alloy AM IN625 specimens after 1000 h exposure at (a,b) 900 °C in lab air and (c,d) 1000 °C in lab air and Ar−4%H_2−2%H_2O gas mixture. (a,c) Thin foils (0.3 mm) are compared with (b,d) thick (2 mm) specimens.

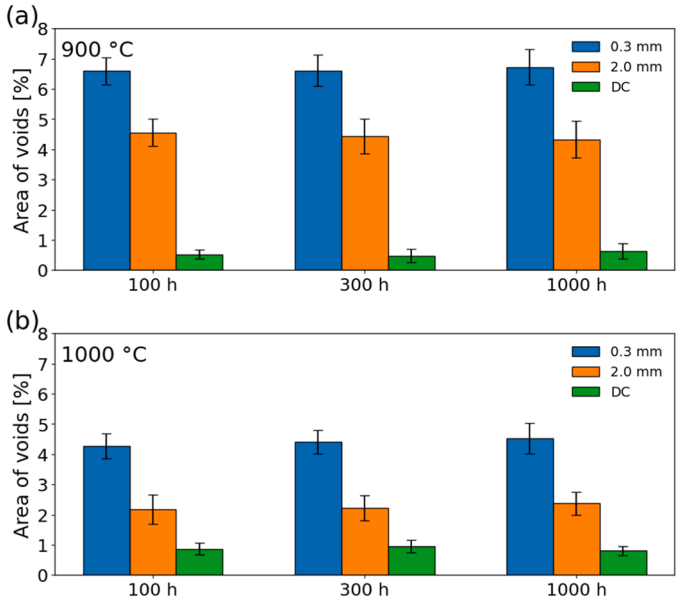

Fig. 9. Average volume fraction of voids in oxidized thin (0.3 mm) and thick (2 mm) alloy AM IN625 specimens as well as in the interdiffusion zones of Ni – AM IN625 diffusion couples (DC) after 100, 300, and 1000 h exposure at (a) 900 °C in lab air and (b) 1000 °C in Ar−4%H_2−2%H_2O. The fractions of voids were determined from low-magnification BSE SEM images.

3.4. Cr depletion profiles

Fig. 10 shows Cr depletion profiles measured with EDX in the CM (Fig. 10a,c) and AM (Fig. 10b,d) alloy IN625 specimens exposed in air (Fig. 10a,b) and Cr/Cr_2O_3 RP (Fig. 10c,d) at 900 °C. In the air exposed specimens, the Cr concentration at the oxide-metal interface in CM is approximately 15 wt% (Fig. 10a), in good agreement with [41], and 17 wt% in AM (Fig. 10b). In AM, the Cr depletion profiles reach deeper into the alloy bulk compared to the respective CM specimens. This difference in the interfacial concentration of Cr between CM and AM along with the deeper Cr depletion in AM signals a faster diffusion of Cr in the AM alloy with respect to CM as discussed in detail in [42]. The Cr profiles in the specimens exposed in RP (Fig. 10c,d) are uniform and do not reveal any Cr loss from the specimens. As Cr is literally not diffusing, there is no significant difference between the Cr profiles measured in AM and CM.

3.5. Interdiffusion experiments

The RP experiments demonstrated that subsurface voids do not appear in the absence of oxidation-induced Cr loss. To further explore the role of diffusion in CM and AM in the formation of the subsurface porosity, two types of experiments were undertaken. Non-oxidation-driven Cr loss was simulated using i) classically welded diffusion couples Ni – IN625 to simulate long-term exposures for up to 1000 h as well as ii) a 5 µm thick Ni-coating electrochemically applied onto IN625.

3.5.1. Diffusion couples

BSE SEM images in Fig. 11 demonstrate the temporal evolution of the interdiffusion zones in the welded diffusion couples Ni-CM and Ni-AM annealed for 100, 300 and 1000 h in vacuum at 900 °C. Similar to the oxidation results in Fig. 4, a precipitate-free zone (PFZ) appears and grows in both CM and AM due to Cr-loss into the nickel. The alloy grains in the PFZ coarsen with time in CM but not in AM. No voids were observed in the Ni-CM diffusion couple up to 1000 h of annealing. In the Ni-AM diffusion couple, some sporadic voids could be seen either in the alloy part of the diffusion couple (bottom row in Fig. 11) or at the welding interface. The voids in the Ni-AM diffusion couples significantly differ from the oxidation-induced voids (compare with bottom row in Fig. 4). First, oxidation produces more cavities (up to 6.5 ± 1.1%) compared to interdiffusion (up to 0.8 ± 0.3%). Second, the voids in the interdiffusion zones are spherical and do not form strings of cavities. Third, unlike the oxidation-induced porosity (Fig. 4), the interdiffusion voids do not exhibit a preferential intergranular morphology and remain predominantly isolated and spherical.

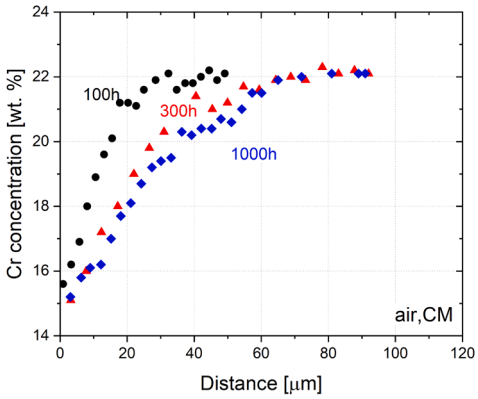

(a)

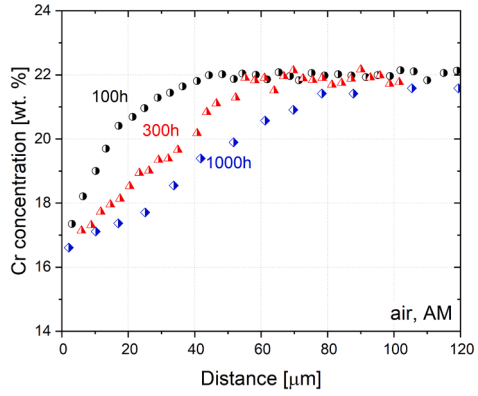

(b)

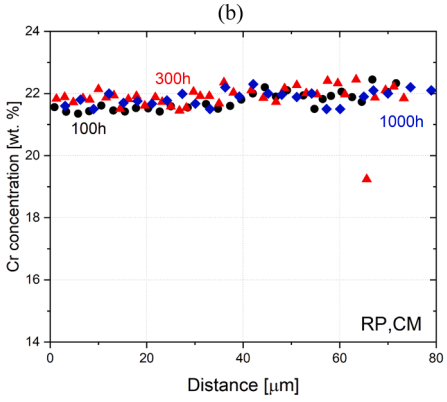

(c)

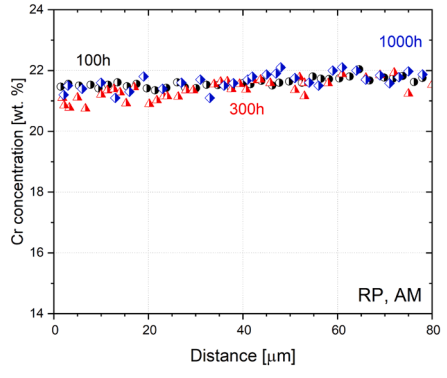

(d)

Fig. 10. Chromium concentration profiles in CM (a,c) and AM (b,d) alloy IN 625 after 100, 300 and 1000 h oxidation in air (a,b) and (c,d) Cr/Cr_2O_3 Rhines pack at 900 °C measured by EDX.

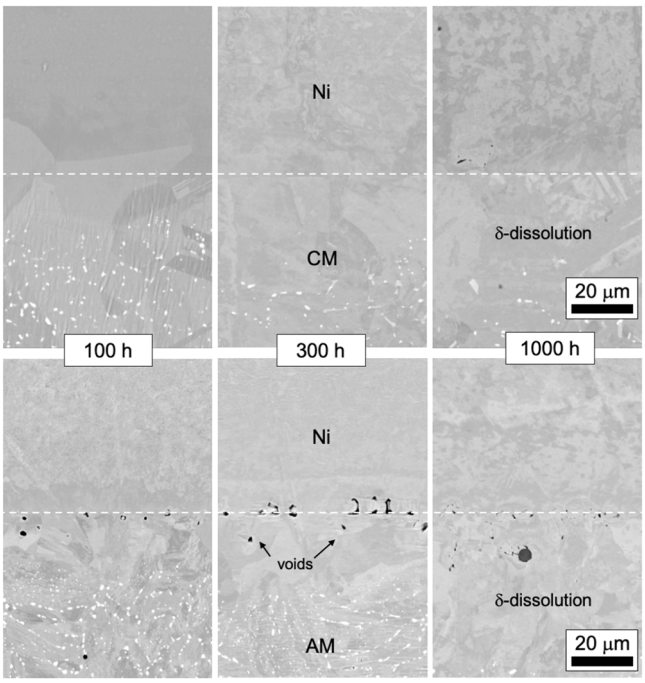

Fig. 11. BSE SEM images of interdiffusion zones in Ni-IN625 (CM and AM) diffusion couples annealed for 100, 300 and 1000 h at 900 °C.

Fig. 12 shows an example of interdiffusion profiles of the main alloying elements in IN625, i.e., Cr, Mo, Nb and Fe, measured with EDX in the Ni-CM (empty symbols) and Ni-AM (full symbols) diffusion couples after annealing for 100 h at 900 °C. The interdiffusion profiles in both CM and AM diffusion couples are classical error-function type distributions. The interdiffusion simulation in DICTRA is in very good agreement with the experimental measurements.

BSE SEM images in Fig. 13 illustrate the difference in void formation induced by interdiffusion (Fig. 13a,b) and oxidation (Fig. 13c,d) in CM (Fig. 13a,c) and AM (Fig. 13b,d) alloy IN625. Similar to the interdiffusion results at 900 °C, no voids formed in the PFZ of CM (Fig. 13a). Sporadic voids could be seen in the interdiffusion zone of the Ni-AM

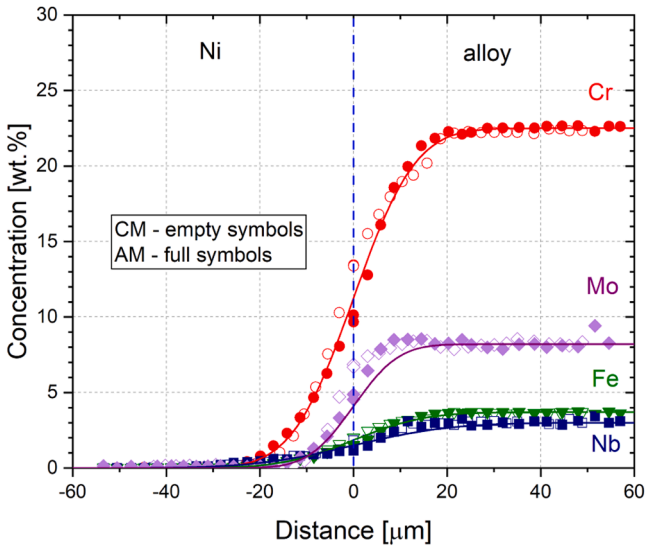

Fig. 12. Concentration profiles of Cr, Mo, Fe and Nb measured with EDX in the interdiffusion zones of Ni-IN625 diffusion couples after 100 h annealing at 900 °C. Full symbols denote AM, empty specimens denote CM, lines are concentration profiles simulated in DICTRA using the TCNi5 and MobNi3 databases.

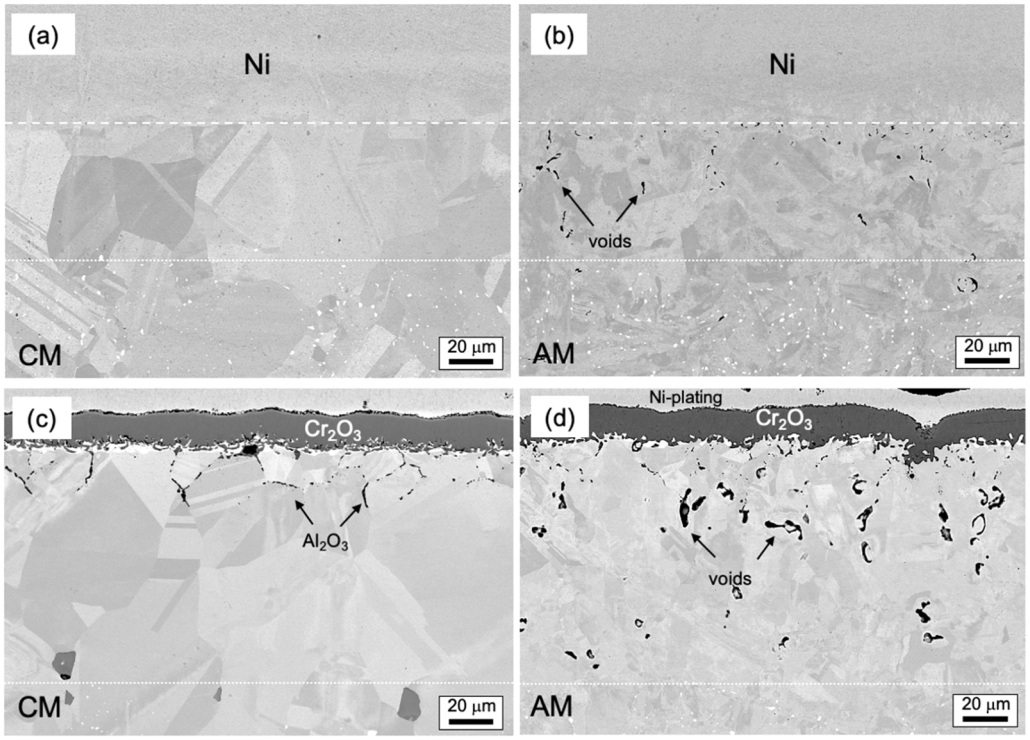

Fig. 13. BSE SEM images comparing void formation in (a,c) CM and (b,d) AM Ni-base alloy IN625 during (a,b) interdiffusion and (c,d) oxidation experiments: 300 h at 1000 °C. Oxidation experiments were carried out in Ar−4%H_2−2%H_2O.

diffusion couples (Fig. 13b). However, oxidation induced significantly more voids in the AM alloy (Fig. 13d). Interestingly, some sporadic spherical pores were also found in the oxidized CM specimen.

The oxidation and interdiffusion experiments can be summarized as

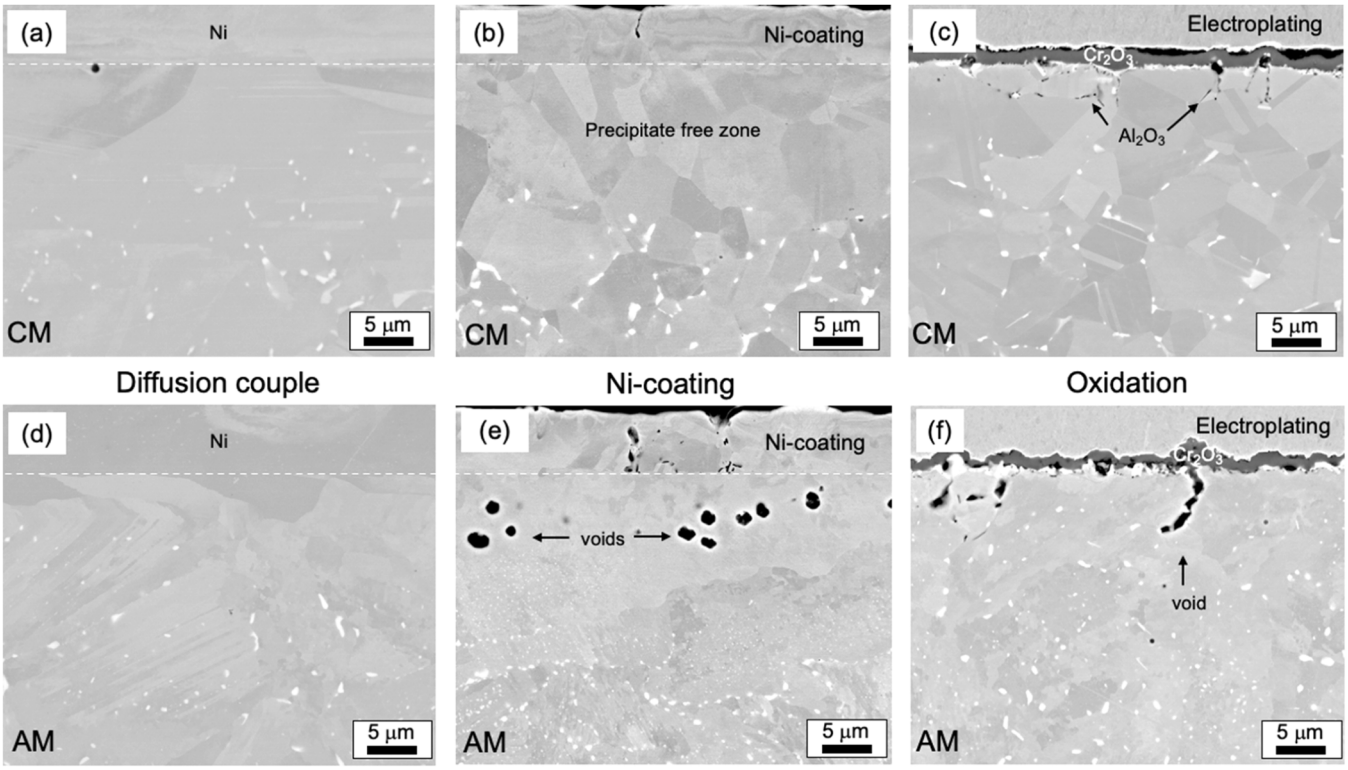

Fig. 14. BSE-SEM images of cross-sectioned (a,d) Ni–IN625 diffusion couples after vacuum annealing, (b,e) electroplated Ni-coated specimens after vacuum annealing, and (c,f) air-oxidized specimens of CM (a–c) and AM (d–f) alloy IN625 after 24 h at 900 °C. Interdiffusion was simulated using (a,d) diffusion couples with an effectively infinite Ni source and (b,e) electroplated Ni coatings providing a finite Ni source. Dashed lines indicate the alloy/Ni interface. The label **Electroplating** denotes the nickel layer deposited during metallographic preparation after the high-temperature exposure.

follows:

i) Neither oxidation nor interdiffusion produced voids in CM IN625 except the oxidation experiments at 1000 °C resulting in a few sporadic pores.
ii) In the AM alloy, oxidation induces significant porosity.
iii) Internal oxidation in Cr/Cr_2O_3 Rhines pack does not lead to porosity. Cr-loss is required to induce the void formation in the Cr-depleted zone.
iv) Cr-loss induced by interdiffusion results only in limited porosity in AM (less than 1 vol%) because the vacancy flux associated with Cr diffusion is largely compensated by the counterdiffusion of Ni from the effectively infinite Ni reservoir.

To experimentally explore the validity of the last statement (iv), interdiffusion experiments were carried out using a finite and thus limited source of Ni. A 5 μm thick layer of Ni was electroplated on the mirror polished surfaces of CM and AM and annealed in vacuum for 24 h at 900 °C. In such a finite diffusion couple, Cr-loss is expected to take place being however not fully compensated by the counter-diffusing Ni as in the classical "infinite" diffusion couples.

3.5.2. Ni-coating vs diffusion couple

Fig. 14 shows BSE SEM micrographs of cross-sectioned Ni-plate–IN625 diffusion couples (Fig. 14a,d) and Ni-coated CM and AM (Fig. 14b,e) IN625 after 24 h vacuum annealing at 900 °C. The interdiffusion zones are compared with the CM and AM alloy IN625 specimens oxidized in air for 24 h at 900 °C (Fig. 14c,f). Similar to the diffusion couples, the Ni-coated CM IN625 specimen (Fig. 14b) reveals a 10 μm thick precipitate free zone (PFZ) which formed due to diffusion of all alloying elements including Cr, Nb and Mo from IN625 into the nickel coating. A PFZ zone is also present in the Ni-coated AM specimen (Fig. 14e). Remarkably, the PFZs in the Ni-coated specimens (Fig. 14b,e) are deeper than the respective PFZs in the oxidized specimens (compare with Fig. 14c,f). Furthermore, no re-precipitation of the δ-phase occurs at the Ni-alloy interface in the diffusion couples and Ni-coated specimens (Fig. 14a-e) compared to the oxidized ones (Fig. 14c,f).

The most important finding in this experiment are the voids in the Ni-coated AM specimen (Fig. 14e). The spherical voids formed in the interdiffusion affected PFZ. Unlike the elongated intergranular voids in the oxidized AM specimen (Fig. 14f and the bottom row in Fig. 4), the randomly distributed voids in the Ni-coated AM specimen did not coalesce at the alloy GBs (Fig. 14f). In the diffusion couples with a thick Ni source (Fig. 14a,d), no void formation was observed after 24 h annealing at 900 °C. However, the long-term diffusion couple experiments (Fig. 11) demonstrate that a small amount of porosity eventually develops in the AM alloy after prolonged annealing, particularly at 1000 °C (Fig. 13d), although its volume fraction remains far below that observed during oxidation.

Fig. 15a shows interdiffusion profiles of Ni and Cr in the Ni – IN625 diffusion couples measured with EDX (full symbols for CM and empty symbols for AM) in the sectioned specimen after 24 h annealing at 900 °C. The measured concentration profiles have the classical error function shape and very well match the concentration profiles simulated in DICTRA [57] using the TCNi5 and MobNi3 databases [58]. The Cr and Ni profiles in the Ni-coated specimens (Fig. 15b) are less steep compared to those in the diffusion couples (Fig. 15a) due to a limited volume of the Ni-coating and, hence, a lower driving force for interdiffusion.

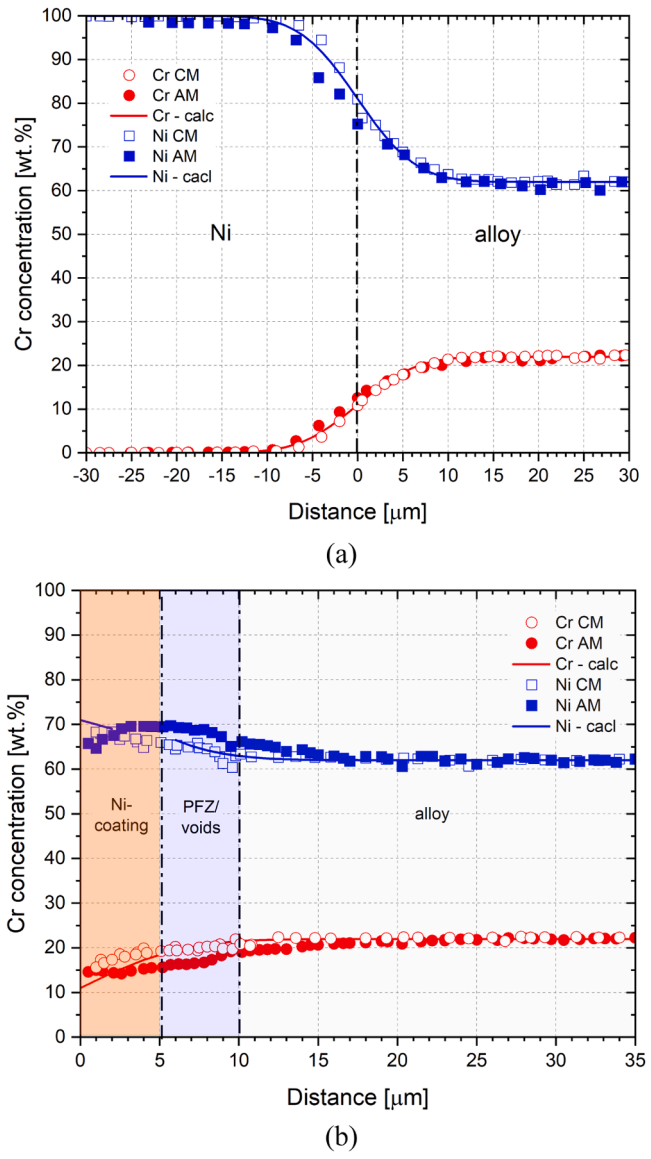

Fig. 15. Concentration profiles of Ni and Cr in interdiffusion zones in (a) Ni-IN 625 diffusion couples and (a) Ni-coated CM and AM alloy IN 625 specimens after 24 h annealing at 900 °C. The concentrations (symbols) were measured with EDX in sectioned specimens demonstrated in Fig. 13. The lines denote simulated concentration profiles calculated using DICTRA with the TCNi5 and MobNi3 databases.

4. Discussion

4.1. Intergranular oxidation attack

4.1.1. General remarks

Intergranular oxidation attack (IGOA) of chromia-forming Ni-base alloys is a corrosion mechanism featured by internal formation of Cr_2O_3 within the subsurface voids in alloys that are designed to form external and protective Cr_2O_3 scales. IGOA needs to be differentiated from the classical internal intergranular oxidation (IGO), e.g., internal oxidation of Al in chromia-forming alloys containing 0.3–0.5 wt% [41,59], and from oxidation of alloy grain boundaries in gases containing water vapor [60–62] and/or carbon-bearing species [63] common for Ni-base alloys at lower temperatures in nuclear application. In summary, IGOA is the intergranular formation of Cr_2O_3 in Ni-base alloys exposed in dry air or oxygen.

IGOA in Ni-base alloys has been discussed in literature since the 1960s and was reported to occur primarily in high-Cr binary Ni-Cr alloys [35,38,64] but also in NiCrAl-base alloys [40] during oxidation in pure oxygen at 1000–1200 °C. The advent of AM Ni-base alloys in the past decade raised again the interest to IGOA as the phenomenon has been systematically reported in the oxidation studies of AM Ni-base alloys [12–38] carried out predominantly in air at 800–1000 °C. The mechanism of IGOA in AM alloys was hypothesized and debated over the past

decade in multiple studies [18–22,30,31] proposing different explanations for the origin of porosity but agreeing on one common point: IGOA and subsurface voids are closely related. To better understand the phenomena behind IGOA, three questions need to be answered:

1) Why do subsurface voids form in AM alloys during oxidation?
2) Why do these voids oxidize?
3) Which factors affect the shape and spatial distribution of the voids?

4.1.2. CM alloys

The early studies of IGOA in model NiCr-base alloys [35,37,38] unanimously agreed on the fact that oxidation of the subsurface cavities was required for IGOA to occur. However, the proposed mechanisms postulated radically different premises. The microcracking hypothesis [37,38] assumed the access of gaseous oxygen through the microcracks in the oxide scale. The mechanism was initially derived to explain the formation of duplex oxide scales via oxidation or sulfidation of the interfacial voids as e.g. summarized by Gibbs in [65] and was supported by experimental evidence provided by Ecer and Meier for Ni−50Cr [37]. On the other hand, Shida et al. [35] rejected the microcracking mechanism and hypothesized that Cr could oxidize in the closed pores due to the pO_2 gradients across the pore. The higher pO_2 was believed to prevail closer to the oxide-metal interface due to a higher Cr depletion and, hence, lower Cr concentration immediately underneath the Cr_2O_3 scale. The latter chemical mechanism seems less convincing for at least two obvious reasons. First, this mechanism would allow the isolated individual in-grain voids to eventually oxidize, which was neither reported in [35] nor in the other afore-mentioned studies.

Second, such a microclimate mechanism would have been intensified in H_2-containing gases because H_2O molecules are well known to act as 'shuttle' species in oxidation–reduction reactions. Hydrogen can reduce oxide at one location while water vapor re-oxidizes the metal at another, thereby facilitating oxygen transport within confined cavities without requiring direct access of molecular oxygen [66]. If such a microclimate mechanism governed oxidation of the subsurface voids, IGOA would therefore be expected to become significantly more pronounced in H_2–H_2O atmospheres. However, the experiments with the Ni22Cr9Mo4Nb model alloy in Ar-H_2-H_2O [22] demonstrated the opposite. The alloy simulating IN625 developed a characteristic IGOA oxide scale morphology during air oxidation, i.e., the Cr_2O_3 scale buckled over the alloy GB which were decorated with strings of GB voids. These voids oxidized and contributed to IGOA. In Ar-H_2-H_2O, the Cr_2O_3 scale adhered much better to the alloy substrate and did not buckle over the GBs. At the same time, both spherical in-grain and elongated GB voids formed in the surface-near region of the alloy. These subsurface voids remained unoxidized for up to 300 h of exposure at 900 °C.

It is noteworthy that an oxide scale morphology very similar to IGOA was observed in the CM alloy batch of IN625 used in the present study by Chyrkin et al. already in [41]. Fig. 16 compares the CM IN625 specimens exposed for 1000 h in air (Figs. 16a,c) and Ar-4%H_2−2%H_2O (Fig. 16b, d) at 1000 °C. In the air exposed specimens (Fig. 16a,c), large intrusions of Cr_2O_3 are visible underneath the outer oxide scale along with the individual spherical voids in the Cr-depleted zone. No such oxide intrusions were found in the specimen exposed in Ar−4%H_2−2%H_2O (Fig. 16b,d) even though the subsurface voids are abundant and locally form consecutive strings.

The complementary BSE, EBSD and EDX analyses presented in Figs. 17 and 18 allow different stages of subsurface void evolution in a thin (0.15 mm) CM IN625 foil shown in Fig. 16d to be distinguished. Due to the pronounced Cr depletion at 1000 °C and the high surface-to-volume ratio of the thin foil, subsurface voids after 1000 h are well resolved. The BSE image (Fig. 17a) reveals both internal Al_2O_3 precipitates and two distinct types of cavities: unoxidized voids and oxidized voids containing internal oxide. The EBSD phase map (Fig. 17b) identifies the internal oxide as Al_2O_3 precipitated along the alloy grain boundaries as well as within the oxidized voids. The corresponding EDX elemental maps (Fig. 17c) further demonstrate enrichment of O, Al and Ti at the walls of the oxidized cavities, confirming the

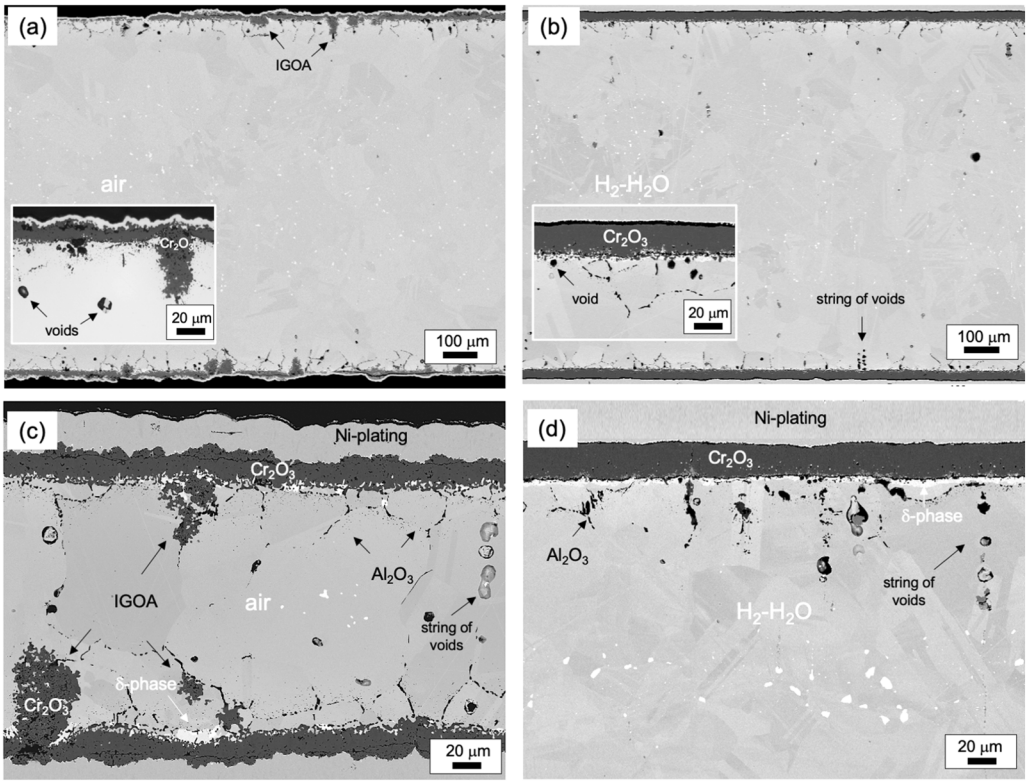

Fig. 16. BSE SEM images of sectioned specimens of CM alloy IN625 after 1000 h exposure at 1000 °C in (a,c) air and (b,d) Ar−4%H_2−2%H_2O. High-magnification insets in (a) and (b) illustrate the details of the oxide scale. The micrographs compare (a,b) 1 mm thick specimens with (c) 0.15 mm and (d) 0.3 mm thick ones.

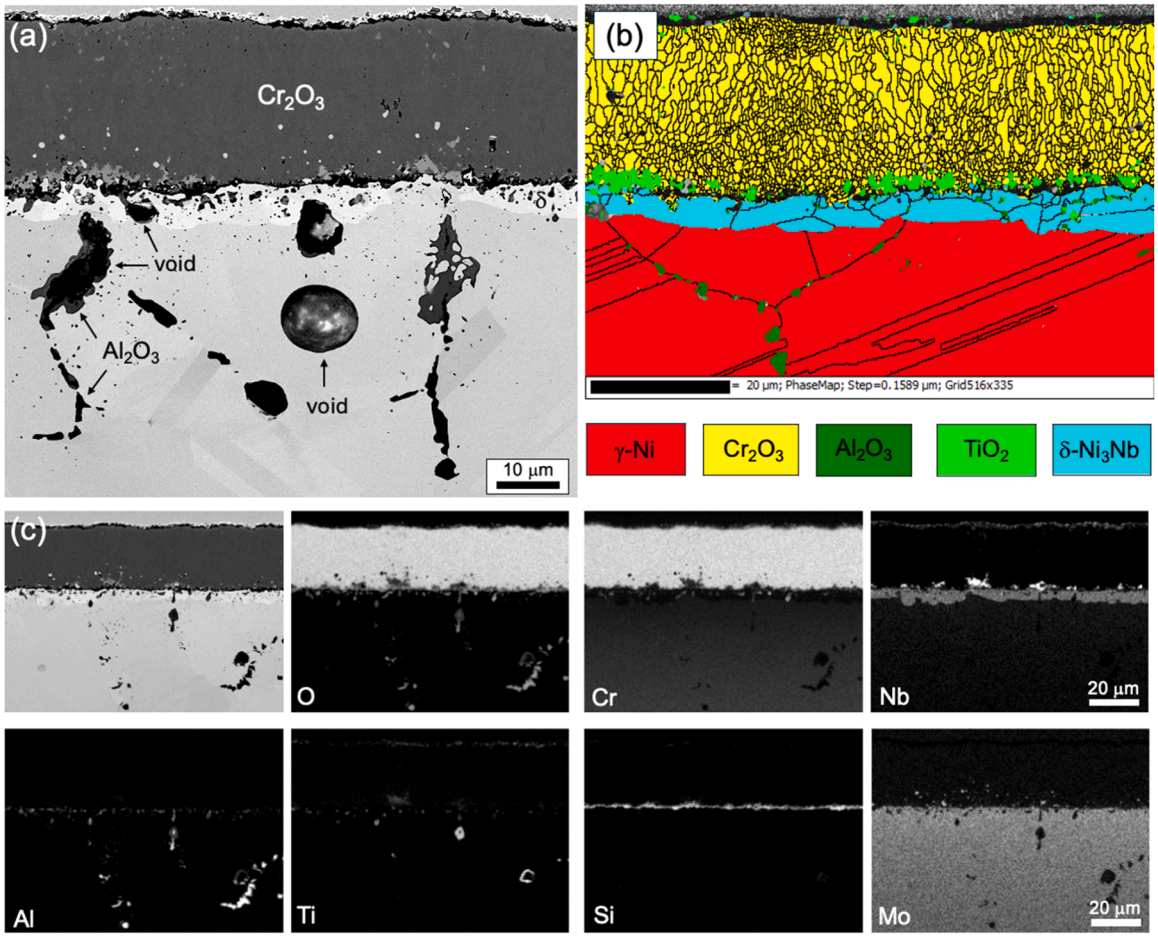

Fig. 17. (a) BSE-SEM image, (b) EBSD phase map and (c) EDX elemental maps of a cross-sectioned 0.15 mm thick CM IN625 specimen after exposure in Ar–4% H_2–2%H_2O for 1000 h at 1000 °C. The combined analyses distinguish unoxidized voids, internal Al_2O_3 precipitates along alloy grain boundaries, and oxidized voids containing Al_2O_3.

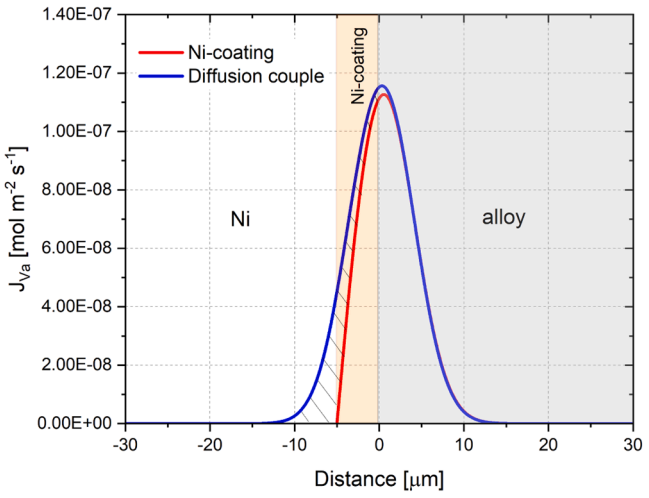

Fig. 18. Spatial distribution of vacancy flux across Ni – IN625 diffusion couple and Ni-coated IN625 after 24 h at 900 °C. Calculated in DICTRA using the TCNi5 and MobNi3 databases. The dashed area corresponds to the excessive vacancy flux arising in Ni-coated IN625.

presence of internal oxide within these voids.

The main difference between the air and Ar−4%H_2−2%H_2O exposures was oxide spallation [41], i.e., Cr_2O_3 adhered very well in Ar−4%H_2−2%H_2O and grew a 25 µm thick scale after 1000 h at 1000 °C while the air exposed specimen systematically revealed a significant mass loss and oxide spallation. Subsurface voids formed in both environments including the characteristic strings of voids or loops as termed by Wood and Hodgkiess [38] (see also 0.15 and 0.3 mm thick specimens in Fig. 16c,d). However, these voids heavily oxidized only in the air exposed specimens because of the intense oxide spallation, oxide cracking and direct permeation of molecular oxygen into the voids while Cr_2O_3 grown in H_2-H_2O remained compact and well-adherent. It should be also noted that no such intrusions were observed at 900 °C, which is presumably due to the absence of subsurface porosity in CM IN625 during oxidation at 900 °C [41]. In summary, the oxide cracking mechanism appears to be the most realistic scenario of IGOA, which will be further confirmed for additively manufactured (AM) alloys in the next sections.

4.1.3. AM alloys

Oxidation-induced subsurface porosity is well-documented for AM Ni-base alloys [12–38] as well as their susceptibility to IGOA. In [18] de Leon Nope et al. discussed the likely triggers of IGOA in AM alloy IN625 mentioning i) preferential attack of some high-angle GBs, ii) differences in alloy chemistry [21,22] and finally suggesting that the formation and the subsequent oxidation of voids was related to the excessive oxygen in the AM alloy due to the atomization process [18]. In other words, this assumption implies that AM alloys are intrinsically prone to subsurface porosity triggered by intensified internal oxidation due to excessive oxygen in the AM alloy. The exact form in which the excessive oxygen

prevails in AM alloys has not been investigated. It is reasonable to assume that it readily reacts with the deoxidants present in the alloys (Al, Mn, Si, Ti) already during the atomization and/or during AM building process and is present in the AM alloy as oxide nanoparticles. This oxygen is already bound and cannot further contribute to internal oxidation. The experiments in Cr/Cr_2O_3 Rhines pack (Fig. 6) vividly demonstrate that internal oxidation is not responsible for the subsurface porosity in the AM alloy. The formation of voids strictly correlates with the depletion of Cr (Fig. 10). Furthermore, Fig. 7 shows that the kinetics of internal Al_2O_3 precipitation is not affected by AM. To summarize, internal oxidation in AM alloy IN625 can be eliminated as a trigger of IGOA. More focus needs to be put thus on external scaling of Cr_2O_3 that continuously depletes the alloy subsurface of Cr, leading to the formation of voids and their eventual oxidation.

In our recent publications [42,67,68], we proposed and validated the oxide decohesion mechanism of IGOA for AM alloy IN625. IGOA was demonstrated to be the interplay between the subsurface porosity and oxide adhesion. As the subsurface porosity is the inevitable consequence of oxidation of the AM alloys, the occurrence of IGOA is determined by whether the Cr_2O_3 scale delaminates and buckles over the GB or not [42]. Introduction of reactive elements (RE) in form of a 10 nm Ce coating significantly improved the adhesion of Cr_2O_3, prevented the oxide scale from buckling and eliminated IGOA: Cr did not oxidize in the closed voids underneath the tightly adherent and compact Cr_2O_3 scale [68]. As discussed for CM alloys above, microcracking of the oxide scale appears to be the most plausible reason for oxidation of the subsurface voids. At the same time, the origin of the abundant subsurface porosity in AM alloys during oxidation is still not fully clear. Therefore, the origin of subsurface porosity in the AM alloy will be separately discussed in the next section.

4.2. Oxidation and vacancy injection

The common denominator for IGOA occurring in CM [35,37,38,59] as well as AM [12–38] chromia-forming Ni-base alloys is the oxidation-induced subsurface porosity [39]. These voids usually form within the Cr-depletion zones underneath the Cr_2O_3 scale either in the alloy grain interior (spherical voids) or at the alloy grain boundaries (strings of spherical voids or elongated cavities). The voids generally form due to the vacancy supersaturation in the alloy surface-near region and nucleate at available sinks, i.e., either surfaces such as GBs and the oxide-metal interface or microdefects and/or inclusions in the alloy microstructure. Two main sources of vacancies discussed in detail in [39] are i) injection of cationic vacancies at the oxide metal interface [69–72] and ii) Kirkendall effect [73–75] due to mismatching diffusivities of the diffusing species, e.g. Cr and Ni in a NiCr-base alloy, and the resulting vacancy flux. The obvious question in this study is what is the exact mechanism of void formation in AM alloys during oxidation: vacancy injection or Kirkendall effect?

Oxidation-induced injection of vacancies into the underlying metal has been lively discussed in literature in the 1960–1970s [69–72] and was recently experimentally confirmed and visualized for high-temperature alloys mainly due to the advent of high-resolution microscopy [76,77] and dual-atmosphere exposure techniques [78]. Vacancy injection was predominantly observed during oxidation of pure metals [70,71,79] but also in selective oxidation of alloys [39,69,77].

When alloy atoms (Cr in the context of the present study) move into the scale, the injected vacancies may undergo several possible fates within the alloy:

1. Vacancies can directly annihilate at dislocations or grain boundaries leading to the metal shrinkage [70,71]. In this scenario, the injected vacancies do not cause void formation.
2. Alternatively, the oxide-metal interface is often the preferential site for the injected vacancies to condense. As demonstrated by Desgranges et al. [39], these interfacial voids can be prevented by cold work which introduces more dislocations into the alloy subsurface and inducing in parallel a recrystallization of the deformed metal.
3. The injected vacancies can diffuse further into the alloy bulk condensing eventually at the alloy GBs or microstructural defects e.g. inclusions. Perusin et al. [78] demonstrated in an elegant dual-atmosphere experiment that the vacancies can migrate throughout the entire thickness of the specimen (1 mm) and annihilate at the non-oxidizing surface of the pure Ni specimen. This effect was achieved by exposing one side of the specimen to $Ar-H_2$ while the other side was oxidizing in air and injecting vacancies.
4. Vacancy injection has been demonstrated to be sensitive to the specimen geometry: the higher surface-to-volume ratio leads to more void formation [70]. This also implies that thin-walled foils have less available alloy volume to accommodate the injected vacancies and thus are more prone to oxidation-induced void formation as in the foils of ferritic stainless steels Sanergy HT [80] or Crofer 22 H [81]. Interestingly, another steel grade Crofer 22 APU in [81] did not reveal void formation in the same experimental conditions. A BCC-to-FCC phase transformation was occurring in Crofer 22 APU but not in Crofer 22 H. Therefore, it is reasonable to assume that a phase transformation and the related volume change offer another possibility to accommodate the injected vacancies.
5. Finally, Stringer stressed in his review [72] the interplay between the vacancy injection and creep of the oxidizing specimens. Plastic deformation and the involved mass transfer may also contribute to annihilation of the supersaturated injected vacancies.

Can vacancy injection be a reasonable explanation of the subsurface porosity (Fig. 4) in AM alloy IN625 in the present study? This question is easy to answer as AM and CM demonstrate essentially the same oxidation kinetics (Fig. 3) and thus the same Cr loss while CM does not reveal any signs of either interfacial or subsurface voids. In other words, CM IN625 can accommodate all vacancies injected in the experiment at 900 °C most likely due to the dissolution and re-precipitation of the δ-phase [41] at the oxide-metal interface (Fig. 4) and the other afore-mentioned mechanisms. At the same time, the AM specimens form voids during oxidation (Fig. 4) in a situation of essentially the same Cr consumption rate (Fig. 3). It is reasonable to assume that the AM alloy cannot accommodate the injected vacancies.

Already in early studies [70,71], vacancy injection was demonstrated to be sensitive to specimen geometry, i.e., the surface-to-volume ratio. Greater condensation of the injected vacancies is expected when the metal cations are removed from a smaller volume of the specimen. Consequently, higher porosity is expected in a thin specimen (tenths of mm) compared to a thick specimen (a few mm), as the smaller metal volume provides fewer opportunities to accommodate the same number of injected vacancies, provided that the oxidation rate is thickness independent.

This effect was clearly observed in the thin foils of AM IN625 (see Fig. 8). The average surface area of voids measured from SEM images was systematically higher in thin (0.3 mm) specimens compared to thick (2 mm) specimens at all temperatures and exposure times (Fig. 9). The volume fraction of voids was higher at 900 °C than at 1000 °C for both thin and thick specimens.

The fraction of injected vacancies that condensed into observable voids was estimated by combining the measured void volume fractions (Fig. 9) with the amount of Cr removed from the alloy, determined from the depletion profiles in Fig. 10b. For the 2 mm thick AM specimens, approximately 0.33 of the injected vacancies condensed into voids after oxidation at 900 °C, whereas this fraction decreased to about 0.24 at 1000 °C. This behavior can be attributed to enhanced vacancy mobility at higher temperatures, which increases the probability of vacancy migration and annihilation within the specimen, whereas at lower temperatures the reduced mobility leads to local vacancy supersaturation and condensation in the near-surface region.

In contrast, the 0.3 mm thick specimens exhibited substantially

higher values of approximately 0.49, irrespective of temperature. These results demonstrate that the oxidation-induced porosity is governed not only by the vacancy injection rate but also by the ability of the underlying alloy to accommodate and annihilate the injected vacancies.

Taken together, the quantitative analysis of vacancy condensation, the thickness-variation experiment (Fig. 8 and Fig. 9), and the interdiffusion experiments (Fig. 11) provide compelling evidence that vacancy injection, rather than the Kirkendall effect, is the dominant mechanism responsible for the formation of oxidation-induced subsurface voids in additively manufactured alloy IN625.

4.3. Role of stresses

In the above discussion, the void formation in alloy 625 is shown to be mainly related to vacancy injection and to a minor extent to the Kirkendall effect. In this section, the role of mechanical stresses [82] arising in the oxide scale during its growth and corresponding stresses in the metal substrate on pore formation is considered.

The oxide growth stress is expected to build up in the scales on high-temperature alloys as the volume of oxide formed is greater than the volume of the metal consumed, expressed as the so-called Pilling-Bedworth-Ratio (PBR). The exact magnitude of the stress depends on several factors including the scale growth rate and mechanism, and on stress relaxation, which might be due to oxide deformation by e.g. creep or (micro)cracking as well as metal deformation by creep or yielding. Creep of metal is believed to be the most important mechanism of relaxation of the oxide growth stresses [72]. In general, during oxidation involving thermal cycling the stresses arising from the mismatch in thermal expansion coefficients between the oxide and the metal must be considered. However, the current experiments were either isothermal or performed under mild cycling conditions (limited number of heating/cooling events with relatively slow air cooling), so thermal stresses are not believed to play a significant role in the void formation.

In the present case, it is very unlikely that the oxide growth stresses per se can cause formation of subsurface porosity in Alloy 625. As the growth stress, which is proportional to the growth rate of the oxide scale, increases with increasing temperature, the corresponding volume of pores in the underlying metal would be expected to increase with temperature as well, especially considering lower metal creep strength, but an opposite effect is observed (compare Fig. 9). Furthermore, for a given test condition (atmosphere, temperature) and sample thickness there is no change in the volume of voids as a function of time, which would be expected if time dependent relaxation of the oxide growth stress by metal creep played a role. The diffusion couple experiments with Ni-coating (Fig. 14f) clearly demonstrate void formation in the underlying AM substrate further confirming that the effect is not related to the growth stress within the scale.

An important observation in the present work was that apart from a minor effect in CM oxidized at 1000 °C there was no obvious effect of specimen thickness on the oxidation rate. Thin specimens (0.1–0.5 mm) of chromia forming ferritic stainless steels were shown to oxidize faster than their 2 mm thick counterparts due to relaxation of the oxide growth stress by metal creep, which was claimed to effectively increase the diffusion coefficients of mobile species across the scale [54,55]. However, ferritic steels have very low intrinsic creep strength and that of IN625 is by far higher due to solid solution and precipitate strengthening δ-phase. In addition, the AM specimens contain very fine precipitates of TiN originating from the alloy or powder manufacturing [83]. This might be the reason why no increase in the oxidation rate was observed with thin sections of AM IN625. For 0.15 mm thick coupon of CM alloy at 1000°C there is less precipitation strengthening due to dissolution of the δ-phase and absence of fine TiN-precipitates so that the specimen exhibits an increase in the oxidation rate compared to the 2 mm thick coupon with a higher strength due to by far greater cross-section.

Cross-sectional SEM analysis in Fig. 4 reveals that the oxide scales grown at 900 °C in air are convoluted on both CM and AM. The convolutions result from compressive oxide growth stresses as observed by other authors in different chromia forming alloy systems (e.g. Cr [84], binary Ni-Cr [56,85]). The high compressive stress during oxidation in dry gases with high pO_2 (air, oxygen) was related to the predominant scale growth mechanism, i.e. a mixed cation-anion transport generating new oxide volume within the previously grown scale. In contrast, the chromia scales formed in H_2/H_2O at 1000 °C appear to be less convoluted compared to those formed during 900°C air oxidation (compare Fig. 4 and Fig. 5). This might be related to a change of the oxide scale growth mechanism in H_2/H_2O towards more inward growth compared to air exposure [56,85]. When comparing the scale morphologies on CM and AM alloy versions grown in H_2/H_2O, the scales on AM appear slightly more convoluted after extended exposure times (300 and 1000 h, compare Fig. 5). At the moment, the exact reason for this minor difference is not fully understood. Possibly it is related to the additional strengthening of AM by the TiN particles as discussed above and consequently impeded creep.

Finally, if the voids open and get oxidized, i.e., filled with chromia, the porosity is expected to extend deeper into the substrate as was observed in the present study during 1000 h air oxidation at 1000°C (compare air with H_2/H_2O in Fig. 16) as well as in our other studies [42,67,68]. Chromia formation inside the subsurface voids puts an additional local stress on the alloy sub-surface regions effectively cleaving the metal and thereby facilitating IGOA. As mentioned in the discussion section “CM alloys” above, after 1000 h oxidation in H_2/H_2O the oxide scale integrity and adherence are much better compared to those in air, which might be (partially) related to the different growth mechanism and thereby lower growth stress. In view of the latter results, higher growth stress within the chromia scale is a factor, which contributes to the oxide delamination and/or cracking and void opening. Measures aimed at suppression of IGOA should consider reduction of the scale growth stress / growth rate e.g. by RE-alloying addition or coating, as suggested in our earlier work [68].

5. Conclusions

The present study leads to three important conclusions:

- Vacancy injection is the dominant mechanism of the oxidation-induced subsurface porosity in the additively manufactured (AM) Ni-base alloy IN625. In contrast to conventionally manufactured (CM) alloys (e.g. wrought or forged), the AM alloy cannot efficiently accommodate the injected vacancies, leading to their condensation primarily along alloy grain boundaries in the Cr-depletion zone.
- The subsurface voids inevitably form in AM alloys during oxidation and may significantly affect the oxidation behavior of the material. If these voids open and become oxidized due to oxide delamination and/or microcracks in the oxide scale, the oxidation process is dominated by intergranular oxidation attack (IGOA). The occurrence of IGOA is governed by the same mechanism in CM and AM IN625: (i) subsurface voids form due to vacancy injection (in CM only above 1000 °C); (ii) poor oxide adhesion and/or defects in the Cr_2O_3 scale facilitate the ingress of molecular oxygen into the voids and their oxidation.
- Compressive stresses in the Cr_2O_3 scales are a significant factor in determining void opening and oxidation. Formation of Cr_2O_3 inside the voids and the resulting volume increase additionally promote void propagation. However, the effect of oxide growth stresses on the void initiation and growth prior to opening is, based on the current results, rather limited or insignificant.

Authors contributions

A.C. conceived and designed this study. A.C. and D.N. systematically discussed the results adjusting the testing program. A.C. carried out experiments and analyses. A.C. wrote the original draft and D.N.

reviewed and edited the manuscript. All authors reviewed the results and approved the final version of the manuscript.

CRediT authorship contribution statement

Dmitry Naumenko: Writing – review & editing, Writing – original draft, Resources, Project administration, Conceptualization. **Anton Chyrkin:** Writing – review & editing, Writing – original draft, Validation, Resources, Project administration, Methodology, Investigation, Funding acquisition, Data curation, Conceptualization.

Declaration of Generative AI and AI-assisted technologies in the writing process

During the preparation of this work, the author used ChatGPT 5.1 (OpenAI) to enhance the graphics of Figures S1 and S2 in the Supplementary Materials, which illustrate the experimental setups for Rhines pack exposures and diffusion welding, respectively. The authors reviewed and edited all content and take full responsibility for the final manuscript.

Declaration of Competing Interest

The authors declare that they have no known competing financial interests or personal relationships that could have appeared to influence the work reported in this paper.

Acknowledgements

This study received no funding. Dr. J.P. Roth and Prof. K. Jahns from Osnabrück University of Applied Science (Osnabrück, Germany) are very kindly acknowledged for providing the AM material, Dr. E. Wessel from Institute for Energy Materials and Devices (IMD−1) at Forschungszentrum Jülich GmbH (Jülich, Germany) for SEM/EBSD analyses.

Appendix A. Supporting information

Supplementary data associated with this article can be found in the online version at doi:10.1016/j.corsci.2026.114147.

Data availability

Data will be made available on request.

References

[1] R.C. Reed, The Superalloys, Cambridge University Press, 2006.
[2] L.E. Murr, Metallurgy of additive manufacturing: examples from electron beam melting, Addit. Manuf. 5 (2015) 40–53.
[3] C.U. Brown, G. Jacob, M. Stoudt, S. Moylan, J. Slotwinski, A. Donmez, Interlaboratory study for nickel alloy 625 made by Laser Powder Bed Fusion to quantify mechanical property variability, J. Mater. Eng. Perform. 25 (2016) 3390–3397.
[4] T. DebRoy, H.L. Wei, J.S. Zuback, et al., Additive manufacturing of metallic components – Process, structure and properties, Prog. Mater. Sci. 92 (2018) 112–224.
[5] G.P. Dinda, A.K. Dasgupta, J. Mazumder, Laser aided direct metal deposition of Inconel 625 superalloy: Microstructural evolution and thermal stability, Mater. Sci. Eng.: A 509 (2009) 98–104.
[6] W.E. Frazier, Metal additive manufacturing: a review, J. Mater. Eng. Perform. 23 (2014) 1917–1928.
[7] K. Son, M.E. Kassner, K.A. Lee, The creep behavior of additively manufactured Inconel 625, Adv. Eng. Mater. (2020) 22.
[8] K.-T. Son, T.Q. Phan, L.E. Levine, et al., The creep and fracture properties of additively manufactured Inconel 625, Mater. (Oxf.) 15 (2021) 101021.
[9] M.E. Kassner, K.T. Son, K.A. Lee, T.-H. Kang, R. Ermagan, The creep and fracture behavior of additively manufactured Inconel 625 and 718, Mater. High. Temp. 39 (2022) 499–506.
[10] S. Sanchez, G. Gaspard, C.J. Hyde, I.A. Ashcroft, G.A.R. Clare, AT. The creep behaviour of nickel alloy 718 manufactured by laser powder bed fusion, Mater. Des. 204 (2021) 109647.
[11] J. Nguejio, F. Szmytka, S. Hallais, A. Tanguy, S. Nardone, M. Godino Martinez, Comparison of microstructure features and mechanical properties for additive manufactured and wrought nickel alloys 625, Materials Science Engineering A 764 (2019) 138214.
[12] D. Monceau, M. Vilasi, High temperature oxidation of additively manufactured structural alloys, JOM 74 (2022) 1659–1667.
[13] T. Galiullin, R. Pillai, W.J. Quadakkers, D. Naumenko, Differences in oxidation behavior of conventionally cast and additively manufactured Co-Base alloy MAR-M-509, High. Temp. Corros. Mater. 100 (2023) 791–816.
[14] M.C. Kuner, M. Romedenne, P. Fernandez-Zelaia, S. Dryepondt, Quantitatively accounting for the effects of surface topography on the oxidation kinetics of additive manufactured Hastelloy X processed by electron beam melting, Addit. Manuf. 36 (2020) 101431.
[15] M. Romedenne, R. Pillai, M. Kirka, S. Dryepondt, High temperature air oxidation behavior of Hastelloy X processed by Electron Beam Melting (EBM) and Selective Laser Melting (SLM), Corros. Sci. 171 (2020) 108647.
[16] M. Romedenne, P. Stack, R. Pillai, S. Dryepondt, Isothermal and cyclic oxidation of Haynes 282 processed by Electron Beam Melting (EBM) and Laser Powder Bed Fusion (LPBF) in dry air at 800 and 950 °C, JOM 74 (2022) 1–12.
[17] S. Dryepondt, M.M. Kirka, F.A. List III, Oxidation behavior of Ni-based alloys fabricated by additive manufacturing, Corros. 2019. Pap. No. C201913558 (2019) 1–13.
[18] G. de Leon Nope, G. Wang, B. Gleeson, Influence of alloy 625 manufacturing process on 950 °C oxidation behavior in air and post-oxidation high-cycle fatigue performance, High. Temp. Corros. Mater. 101 (2024) 1167–1179.
[19] G. de Leon Nope, G. Wang, J.M. Alvarado-Orozco, B. Gleeson, Effects of high-temperature oxidation on fatigue life of additive-manufactured alloy 625, Miner. Met. Mater. Ser. (2023) 249–269.
[20] G. de Leon Nope, G. Wang, J.M. Alvarado-Orozco, B. Gleeson, Role of elemental segregation on the oxidation behavior of additively manufactured alloy 625, JOM 74 (2022) 1698–1706.
[21] A. Chyrkin, K.O. Gunduz, I. Fedorova, et al., High-temperature oxidation behavior of additively manufactured IN625: effect of microstructure and grain size, Corros. Sci. (2022) 205.
[22] A. Chyrkin, W.J. Nowak, K.O. Gunduz, et al., Intergranular oxidation of additively manufactured Ni-base alloy 625: the role of Si, Corros. Sci. 219 (2023) 111234.
[23] S. Parizia, G. Marchese, M. Rashidi, et al., Effect of heat treatment on microstructure and oxidation properties of Inconel 625 processed by LPBF, J. Alloy. Compd. 846 (2020) 156418.
[24] K.Y. Pineda-Arriaga, J.H. Ramírez-Ramírez, F.A. Pérez-González, J.M. Alvarado-Orozco, R. Colás, N.F. Garza-Montes-de-Oca, Oxidation in water vapor of Inconel 625 fabricated by additive manufacturing, High. Temp. Corros. Mater. 101 (2024) 1–11.
[25] K.Y. Pineda-Arriaga, J.H. Ramírez-Ramírez, F.A. Pérez-González, J.M. Alvarado-Orozco, R. Colás, N.F. Garza-Montes-de-Oca, Characterization of the high-temperature oxidation behavior of Inconel 625® fabricated by additive manufacturing and conventional methods, Oxid. Met. 98 (2022) 489–510.
[26] M. Sharifitabar, S. Khorshahian, M. Shafiee Afarani, P. Kumar, N.K. Jain, High-temperature oxidation performance of Inconel 625 superalloy fabricated by wire arc additive manufacturing, Corros. Sci. 197 (2022) 110087.
[27] B.W. Andrade, F.E. Mariani, R.T. Coelho, A.M. de Sousa Malafaia, Comparison of the oxidation behavior at high temperature of INCONEL 625 forged and produced by additive manufacturing, High. Temp. Corros. Mater. (2024) 1–14.
[28] M.R. Condruz, G. Matache, A. Paraschiv, T. Badea, V. Badilita, High temperature oxidation behavior of Selective Laser Melting manufactured IN 625, Met. (Basel) 10 (2020) 668.
[29] S. Madhusudan, E. Epifano, J. Favergeon, T. Sanviemvongsak, D. Maréchal, D. Monceau, High temperature intergranular oxidation of nickel based superalloy inconel 718, High. Temp. Corros. Mater. 101 (2024) 873–884.
[30] T. Sanviemvongsak, D. Monceau, C. Desgranges, B. Macquaire, Intergranular oxidation of Ni-base alloy 718 with a focus on additive manufacturing, Corros. Sci. 170 (2020) 108684.
[31] T. Sanviemvongsak, D. Monceau, B. Macquaire, High temperature oxidation of IN 718 manufactured by laser beam melting and electron beam melting: effect of surface topography, Corros. Sci. 141 (2018) 127–145.
[32] T. Sanviemvongsak, D. Monceau, M. Madelain, C. Desgranges, J. Smialek, B. Macquaire, Cyclic oxidation of alloy 718 produced by additive manufacturing compared to a wrought-718 alloy, Corros. Sci. 192 (2021) 109804.
[33] J.H. Weber, P.S. Gilman, Environmentally induced porosity in Ni-Cr and Ni-Cr oxide dispersion strengthened alloys, Scr. Metall. 18 (1984) 479–482.
[34] A.H. Rosenstein, J.K. Tien, W.D. Nix, Void formation in INCONEL MA-754 by high temperature oxidation. Metallurgical transactions, Phys. Metall. Mater. Sci. (1986) 151–162.
[35] Y. Shida, G.C. Wood, F.H. Stott, D.P. Whittle, B.D. Bastow, Intergranular oxidation and internal void formation in Ni-40% Cr alloys, Corros. Sci. 21 (1981) 581–597.
[36] Y.X. Xu, J.T. Lu, X.W. Yang, J.B. Yan, W.Y. Li, Effect and role of alloyed Nb on the air oxidation behaviour of Ni-Cr-Fe alloys at 1000 °C, Corros. Sci. 127 (2017) 10–20.
[37] G.M. Ecer, G.H. Meier, Oxidation of high-chromium Ni-Cr alloys, Oxid. Met. 13 (1979) 119–158.
[38] G.C. Wood, T. Hodgkiess, Characteristic Scales on Pure Nickel-Chromium Alloys at 800°–1200°C, J. Electrochem. Soc. 113 (1966) 319.
[39] C. Desgranges, F. Lequien, E. Aublant, M. Nastar, D. Monceau, Depletion and voids formation in the substrate during high temperature oxidation of Ni-Cr alloys, Oxid. Met. 79 (2013) 93–105.

[40] F.H. Stott, G.C. Wood, Y. Shida, D.P. Whittle, B.D. Bastow, The development of internal and intergranular oxides in nickel-chromium-aluminium alloys at high temperature, Corros. Sci. 21 (1981) 599–624.
[41] A. Chyrkin, P. Huczkowski, V. Shemet, L. Singheiser, W.J. Quadakkers, Sub-scale depletion and enrichment processes during high temperature oxidation of the nickel base alloy 625 in the temperature range 900-1000 °c, Oxid. Met. (2011) 75.
[42] A. Chyrkin, J.-P. Roth, D. Naumenko, K. Jahns, Does additive manufacturing cause intergranular oxidation attack of high-temperature alloys? Case study of Ni-base alloy IN625, Corros. Sci. 260 (2026) 113588.
[43] A. Kreitcberg, V. Brailovski, S. Turenne, Effect of heat treatment and hot isostatic pressing on the microstructure and mechanical properties of Inconel 625 alloy processed by laser powder bed fusion, Mater. Sci. Eng. A 689 (2017) 1–10.
[44] G. Marchese, S. Parizia, M. Rashidi, et al., The role of texturing and microstructure evolution on the tensile behavior of heat-treated Inconel 625 produced via laser powder bed fusion, Mater. Sci. Eng. A 769 (2020) 138500.
[45] F. Rhines, W. Johnson, W. Anderson, Rates of high-temperature oxidation of dilute copper alloys, Trans. Metall. Soc. Aime. 147 (1942) 205–221.
[46] D. Jullian, A. Prillieux, D.B. Hibbert, J. Zhang, D.J. Young, Internal oxidation of austenitic Fe-Ni-Cr alloys at high temperatures: deduction of oxygen permeability and the influence of carbon-bearing gases, Corros. Sci. 224 (2023) 111465.
[47] D. Jullian, A. Prillieux, J. Zhang, D.J. Young, Oxygen permeability of Fe-Ni-Cr alloys at 1100 and 1150 °C under carbon-free and carbon-containing gases, Mater. Corros. 68 (2017) 197–204.
[48] A. Prillieux, D. Jullian, J. Zhang, D. Monceau, D.J. Young, Internal oxidation in dry and wet conditions for oxygen permeability of Fe–Ni alloys at 1150 and 1100 °C, Oxid. Met. 87 (2017) 273–283.
[49] A. Chyrkin, C. Cossu, J.-E. Svensson, J. Froitzheim, Internal Oxidation of a Fe–Cr Binary Alloy at 700–900 °C: The Role of Hydrogen and Water Vapor, Oxid. Met. 98 (2022) 273–289.
[50] E. Schmucker, C. Petitjean, L. Martinelli, P.J. Panteix, B. Lagha, M. Vilasi, Oxidation of Ni-Cr alloy at intermediate oxygen pressures. II. Towards the lifetime prediction of alloys, Corros. Sci. 111 (2016) 467–473.
[51] A. Chyrkin, W.J. Quadakkers, Effect of α-to-γ transformation on internal oxidation in FeCr-base alloys in dry and wet gases, J. Alloy. Compd. 1045 (2025) 184722.
[52] G. Gulsoy, G.S. Was, Mechanism of Internal Oxidation of Alloy 617 in He-CO-CO2 Environments at 1123 K (850 °C), Metall. Mater. Trans. A Phys. Metall. Mater. Sci. 46 (2015) 525–535.
[53] M.H. Ani, T. Bin Kodama, M. Ueda, K. Kawamura, T. Maruyama, The effect of water vapor on high temperature oxidation of Fe-Cr alloys at 1073 K, Mater. Trans. 50 (2009) 2656–2663.
[54] P. Huczkowski, S. Ertl, J. Piron-Abellan, et al., Effect of component thickness on lifetime and oxidation rate of chromia forming ferritic steels in low and high pO_2 environments, Mater. High. Temp. 22 (2005) 253–262.
[55] C. Asensio-Jimenez, L. Niewolak, H. Hattendorf, et al., Effect of specimen thickness on the oxidation rate of high chromium ferritic steels: The significance of intrinsic alloy creep strength, Oxid. Met. 79 (2013) 15–28.
[56] J. Zurek, G.H. Meier, E. Essuman, M. Hänsel, L. Singheiser, W.J. Quadakkers, Effect of specimen thickness on the growth rate of chromia scales on Ni-base alloys in high- and low-pO2 gases, J. Alloy. Compd. 467 (2009) 450–458.
[57] A. Borgenstam, A. Engström, L. Höglund, J. Ågren, DICTRA, a tool for simulation of diffusional transformations in alloys, J. Phase Equilibria 21 (2000) 269–280.
[58] Bratberg J., Mao H., Kjellqvist L., Engström A., Mason P., Chen Q. The development and validation of a new thermodynamic database for Ni-based alloys. 2012;
[59] Y. Shida, T. Moroishi, Oxidation behaviour of alloy 800 in an impure helium atmosphere at high temperatures, Corros. Sci. 33 (1992) 211–224.
[60] K. Kruska, M.J. Olszta, J. Wang, D.K. Schreiber, Intergranular corrosion of Ni-30Cr in high-temperature hydrogenated water after removing surface passivating film, npj Mater. Degrad. 2024 81 8 (2024) 1–10.
[61] S.M. Bruemmer, M.J. Olszta, M.B. Toloczko, D.K. Schreiber, Grain boundary selective oxidation and intergranular stress corrosion crack growth of high-purity nickel binary alloys in high-temperature hydrogenated water, Corros. Sci. 131 (2018) 310–323.
[62] L. Luo, M. Su, P. Yan, et al., Atomic origins of water-vapour-promoted alloy oxidation, Nat. Mater. 17 (2018) 514–518.
[63] M. Weiser, M.J. Olszta, M.H. Engelhard, Z. Zhu, D.K. Schreiber, Visualizing oxygen transport pathways during intergranular oxidation in Ni-Cr, npj Mater. Degrad. 2023 71 7 (2023) 1–11.
[64] G.C. Wood, T. Hodgkiess, Characteristic Scales on Pure Nickel-Chromium Alloys at 800°–1200°C, J. Electrochem. Soc. 113 (1966) 319.
[65] G.B. Gibbs, A model for mild steel oxidation in CO2, Oxid. Met. 7 (1973) 173–184.
[66] A. Rahmel, J. Tobolski, Einfluss von Wasserdampf und Kohlendioxyd auf die Oxydation von Nickel in Sauerstoff bei hohen Temperaturen, Corros. Sci. 5 (1965) 815–820.
[67] A. Chyrkin, A. Fazi, M. Sattari, et al., Oxidation of additively manufactured Ni-base alloy IN625: Mechanism of intergranular oxidation, Corros. Sci. 256 (2025) 113218.
[68] A. Chyrkin, A. Fazi, M. Sattari, et al., PVD Ce-coating to mitigate intergranular oxidation of additively manufactured Ni-base alloy IN625, npj Mater. Degrad. 2025 91 9 (2025) 1–13.
[69] D.L. Douglass, The oxidation mechanism of dilute Ni-Cr alloys, Corros. Sci. 8 (1968) 665–678.
[70] R. Hales, A.C. Hill, The role of metal lattice vacancies in the high temperature oxidation of nickel, Corros. Sci. 12 (1972) 843–853.
[71] G.B. Gibbs, R. Hales, The influence of metal lattice vacancies on the oxidation of high temperature materials, Corros. Sci. 17 (1977) 487–507.
[72] J. Stringer, Stress generation and relief in growingoxide films, Corros. Sci. 10 (1970) 513–543.
[73] A.D. Smigelskas, E.O. Kirkendall, Diffusion of zinc in alpha-brass, Trans. Aime. 147 (1942) 104–110.
[74] H.B. Huntington, F. Seitz, Mechanism for self-diffusion in metallic copper, Phys. Rev. 61 (1942) 315.
[75] C. Salsi, J. Lesseur, D. Monceau, C. Desgranges, T. Gheno, Time evolution of Kirkendall porosity in single-phase Ni-based diffusion couples, Acta Mater. 293 (2025) 121022.
[76] C.M. Wang, A. Genc, H. Cheng, L. Pullan, D.R. Baer, S.M. Bruemmer, In-Situ TEM visualization of vacancy injection and chemical partition during oxidation of Ni-Cr nanoparticles, Sci. Rep. 2014 41 4 (2014) 1–6.
[77] R.P. Oleksak, M. Kapoor, D.E. Perea, G.R. Holcomb, Ö.N. Doğan, The role of metal vacancies during high-temperature oxidation of alloys, npj Mater. Degrad. 2018 21 2 (2018) 1–8.
[78] S. Perusin, B. Viguier, D. Monceau, L. Ressier, E. Andrieu, Injection of vacancies at metal grain boundaries during the oxidation of nickel, Acta Mater. 52 (2004) 5375–5380.
[79] J.E. Harris, Vacancy injection during oxidation—A re-examination of the evidence, Acta Metall. 26 (1978) 1033–1041.
[80] R. Sachitanand, J.E. Svensson, J. Froitzheim, The Influence of Cr Evaporation on Long Term Cr Depletion Rates in Ferritic Stainless Steels, Oxid. Met. 84 (2015) 241–257.
[81] A. Chyrkin, J. Froitzheim, Premature breakaway oxidation of ferritic stainless steels triggered by austenitization, Corros. Sci. 256 (2025) 113260.
[82] H.E. Evans, Stress effects in high temperature oxidation of metals, Int. Mater. Rev. 40 (1995) 1–40.
[83] R. Hu, X. Liu, Z. Hang, K. Zhang, B. Jiang, X. Luo, Laser additive manufacturing of a TiN strengthened nickel-based superalloy with tailored microstructure and tensile performance, Mater. Sci. Eng. A 940 (2025) 148569.
[84] M. Michalik, S.L. Tobing, M. Hänsel, V. Shemet, W.J. Quadakkers, D.J. Young, Effects of water vapour on the high temperature nitridation of chromium, Mater. Corros. 65 (2014) 260–266.
[85] E. Essuman, G.H. Meier, J. Zurek, et al., Effect of oxygen partial pressure on the oxidation behaviour of an yttria dispersion strengthened NiCr-base alloy, J. Mater. Sci. 43 (2008) 5591–5598.